

# Magnetolectric microelectromechanical and nanoelectromechanical systems for the IoT

Bin Luo<sup>1,7</sup>, A. R. Will-Cole<sup>2,7</sup>, Cunzheng Dong<sup>1</sup>, Yifan He<sup>1</sup>, Xiaxin Liu<sup>1</sup>, Hwaider Lin<sup>3</sup>, Rui Huang<sup>1</sup>, Xiaoling Shi<sup>3</sup>, Michael McConney<sup>4</sup>, Michael Page<sup>4</sup>, Mohan Sanghadasa<sup>5</sup>, Ramamoorthy Ramesh<sup>6</sup> & Nian X. Sun<sup>1</sup>✉

## Abstract

The internet of things (IoT) has revolutionized society by creating a network of interconnected devices with sensors, processing ability and software for data exchange. However, the expansion of IoT places undue strain on energy resources. Thus, the development of low-power components is critical. Moreover, the demand for IoT has opened new markets for wearable technologies, necessitating innovations towards miniaturization. This rapid growth introduces further challenges in communication and environmental adaptability. Magnetolectric (ME) microelectromechanical and nanoelectromechanical systems (M/NEMS) introduce unparalleled properties to reshape the IoT landscape. ME M/NEMS enable a 100,000× reduction in wavelength, resulting in reduced size and weight, and provide multifunctionality, such as simultaneous sensing, data transmission and wireless power transfer. With renewed interest in ME M/NEMS platforms, several disruptive technologies have emerged ranging from ultra-compact radiofrequency front-ends to quantum sensing, computing and communication networks. This Review delves into ME materials, ME composites and ME M/NEMS for IoT functions, including logic memory; magnetic sensing; wireless power transfer; ultra-compact antennas; power, radiofrequency and microwave electronics; and communication systems.

## Sections

Introduction

ME materials and composites

ME-based memory and logic

ME-based magnetometers

ME antennas

ME WPT

MEs for power, RF and microwave electronics

Emerging systems

Outlook

<sup>1</sup>W.M. Keck Laboratory for Integrated Ferroics, Electrical and Computer Engineering Department, Northeastern University, Boston, MA, USA. <sup>2</sup>Microsystems, Engineering, Science, and Applications, Sandia National Laboratories, Albuquerque, NM, USA. <sup>3</sup>Winchester Technologies, LLC, Burlington, MA, USA. <sup>4</sup>Materials Directorate, Air Force Research Laboratory, Dayton, OH, USA. <sup>5</sup>DEVCOM Aviation & Missile Center, Army Futures Command, Huntsville, AL, USA. <sup>6</sup>Materials Science and Nanoengineering, and Physics and Astronomy, Rice University, Houston, TX, USA. <sup>7</sup>These authors contributed equally: Bin Luo, A. R. Will-Cole. ✉e-mail: [n.sun@northeastern.edu](mailto:n.sun@northeastern.edu)

## Key points

- Magnetolectric (ME) microelectromechanical and nanoelectromechanical systems (M/NEMS) hold the promise to revolutionize the internet of things by addressing critical challenges in size, energy efficiency, communication and adaptability to challenging environments.
- ME materials and composites enable the electrical control of magnetism, leading to magnetolectric, spin-orbit-coupled logic devices and ME random access memories for attojoule-class nonvolatile information storage and modern computing.
- ME M/NEMS enable ultra-compact antennas with improved efficiency for simultaneous wireless information and power transfer and smart sensor nodes with reduced cost, size, weight and power compared with conventional electrical counterparts.
- Voltage-tunable ME inductors, circulators and phase shifters based on electrical field tuning permeability, spin wave, Young's modulus and wideband magnetoacoustic devices with giant nonreciprocity provide excellent opportunities for compact, lightweight and power-efficient radiofrequency (RF), microwave and power electronics.
- ME M/NEMS show great potential for high-gain ME antennas and ultra-sensitive ME sensors in a strong coupling region, effectively controlling quantum defects and very-low-frequency (VLF) mobile bi-directional underground and underwater communication.
- Challenges exist in the CMOS-compatible integration of ME materials and far-field VLF communication with ME antennas despite superior energy efficiency, low power loss, ultra-compact size and outstanding multifunctionality and versatility.

## Introduction

The internet of things (IoT) is a network of interconnected devices and objects that collect, communicate and exchange information autonomously. It has permeated numerous sectors of modern life, from smart homes and wearable gadgets to industrial automation and health-care monitoring. The proliferation of IoT devices necessitates solutions that address key challenges, including compact form factors, energy efficiency, seamless communication and adaptability to diverse environments<sup>1</sup>. Magnetolectric (ME) materials, composites and devices offer unique functionalities and capabilities that can revolutionize the landscape of IoT technologies.

ME systems are composed of engineered materials and composites with strong direct magnetolectric coupling and converse magnetolectric coupling. The origin of ME materials traces back to the discovery and exploration of single-phase ME materials from the late nineteenth century through the mid-twentieth century. In the 1970s, scientists at the Philips Research Laboratories studied ME composites based on *in situ* grown eutectic piezoelectric and ferrite materials, setting the groundwork for subsequent developments in ME composites and devices<sup>2,3</sup>. In 2001, the demonstration of the strong ME coupling of piezoelectric-magnetostrictive laminate composites ignited an exponential growth of research and development on ME materials and devices<sup>4,5</sup>, encompassing applications such as ME-based magnetic field

sensors, memory and logic components, and power, radiofrequency (RF) and microwave applications, antennas and filters<sup>2–32</sup> (Fig. 1).

ME sensors can detect magnetic fields on the order of fT at room temperature<sup>19</sup> and enable ultra-compact ME mechanical antennas for mobile bi-directional very-low-frequency (VLF) communications<sup>29,30</sup>. Furthermore, ME devices show enhanced efficiency for wireless power transfer (WPT) over state-of-the-art resonant coils and have the potential to facilitate simultaneous wireless information and power transfer<sup>26</sup>. Leveraging distinct acoustic resonance modes, simultaneous magnetic field sensing, VLF, RF and microwave communications, and WPT have been experimentally demonstrated<sup>26</sup>.

One of the prominent advantages of ME devices, especially for mechanical antennas, is their ultra-compact size. Because ME antennas operate at their electromechanical resonance, their size is comparable to the mechanical wavelength rather than the electromagnetic wavelength. Being that the mechanical wavelength is  $10^{-5}$  the magnitude of the electromagnetic wavelength, ultra-miniaturized RF components are permitted<sup>32</sup>. This reduction in size is beneficial for IoT systems wherein space constraints dictate device designs. Together with ME WPT, ME energy harvesters can power IoT nodes using ambient mechanical vibrations, and magnetic and electric fields, reducing dependence on traditional power sources and prolonging the operational lifespan of battery-powered devices. From improved efficiency and compact sizes to magnetic field sensing and data processing, ME technologies can reshape the IoT landscape, propelling its evolution towards a streamlined, interconnected, and intelligent ecosystem.

In this Review, we provide a foundational understanding of the cutting-edge progress in piezoelectric and magnetic materials for ME composites and discuss their application in memory and logic devices<sup>33</sup>, such as magnetolectric spin-orbit (MESO)-coupled logic devices<sup>34</sup>. Then we present a range of ME microelectromechanical and nanoelectromechanical systems (M/NEMS) relevant to IoT applications<sup>22,26,31,32</sup>, such as magnetic field sensing for wearable medical devices<sup>26</sup>, antennas designed for both ultra-high-frequency (UHF, 0.3–3 GHz)<sup>22,31</sup> and very-low-frequency (VLF, 3–30 kHz) bands<sup>29,30</sup>, and wireless power transfer<sup>26</sup>. Furthermore, we highlight ME-tunable RF components<sup>35,36</sup> and introduce pioneering devices such as acoustic-driven ferromagnetic magnetic resonance (ADFMR)<sup>37</sup> for nonreciprocal RF devices<sup>25,28</sup>, quantum transduction and control<sup>38–40</sup>, and VLF antenna arrays<sup>29,41</sup> for underground and underwater communications. Finally, we present a prospective analysis of the highlights and challenges of the use of ME M/NEMS systems in IoT.

## ME materials and composites

Strain-mediated ME coupling is a dominant mechanism to describe ME coupling<sup>42</sup>. Strain-mediated ME laminates composed of piezoelectric and magnetostrictive materials demonstrate much higher ME coupling strength (ME coupling on the order of hundreds of  $\text{mV cm}^{-1} \text{Oe}^{-1}$ ) than single-phase multiferroic materials (two or more ferroic properties, such as ferromagnetism, antiferromagnetism, ferrimagnetism, ferroelectricity, antiferroelectricity, ferroelasticity and ferrotoroidicity), such as bismuth ferrite ( $\text{BiFeO}_3$ , BFO has an ME coupling of  $-0.064 \text{ mV cm}^{-1} \text{Oe}^{-1}$ )<sup>32,43</sup>. For bulk laminate composites, the theoretical ME voltage coefficient  $\alpha_{\text{ME}}^{L-L}$  for the longitudinal-longitudinal (L-L) mode is given by equation (1):

$$\alpha_{\text{ME}}^{L-L} = \frac{nd_{33,m}g_{33,p}}{ns_{33}^E(1-k_{33}^2) + (1-n)s_{33}^H} \quad (1)$$

where  $s_{33}^E$  and  $s_{33}^H$  are the elastic compliances of the piezoelectric and magnetostrictive layers, respectively;  $k_{33}$  is the electromechanical coupling coefficient of the piezoelectric layer;  $n$  is the ratio of magnetic layer thickness to the total thickness of the ME laminate;  $d_{33,m}$  and  $g_{33,p}$  are the longitudinal piezomagnetic and piezoelectric coefficients, respectively<sup>13</sup>.

The assumption here is that the interfacial coupling coefficient is equal to 1. The interface between the magnetic and piezoelectric phases is perfectly bonded and enables strain transfer without appreciable loss. Additionally, it is assumed that there is no dielectric, piezoelectric, and mechanical loss in the composite. The ME voltage coefficient depends on the electromechanical and magnetomechanical properties of the piezoelectric and ferromagnetic layers.

The magnetic material in the ME composites should have high magnetostriction (>70 ppm), high piezomagnetic coefficient (>10 ppm Oe<sup>-1</sup>), near unity magnetomechanical coupling factor, and low loss (ferromagnetic resonance linewidth <20 Oe in X-band)<sup>14</sup>. High ME coupling has been achieved in magnetic alloys, such as (Fe<sub>80</sub>Ga<sub>20</sub>)<sub>88</sub>B<sub>12</sub> (ref. 14), or ferrite films<sup>16</sup> grown on single crystal ferroelectric substrates, namely Pb(Zn<sub>1/3</sub>Nb<sub>2/3</sub>)O<sub>3</sub>-PbTiO<sub>3</sub> (PZN-PT) or Pb(Mg<sub>1/3</sub>Nb<sub>2/3</sub>)O<sub>3</sub>-PbTiO<sub>3</sub> (PMN-PT), enabling high mechanical resonance quality factor ( $Q_{MR}$ ), low-frequency devices<sup>17,44–47</sup>. However, the large electric fields (8 kV cm<sup>-1</sup> translating to 400 V for 0.5-mm-thick ferroelectric slab) required to tune the magnetization are not feasible for most working devices<sup>44</sup>. Additionally, the single-crystal ferroelectrics are not easily integrated onto Si substrates owing to back-end-of-line complementary metal-oxide-semiconductor (CMOS) processing incompatibility (that is crystallization temperature higher than 450 °C), and the requirement of lattice matching for epitaxy. Thin film ME heterostructures have been integrated with CMOS-compatible processes on Si using piezoelectric films, such as AlN, ZnO, Al<sub>0.73</sub>Sc<sub>0.27</sub>N, coupled to magnetostrictive alloy films, such as (Fe<sub>80</sub>Ga<sub>20</sub>)<sub>88</sub>B<sub>12</sub> or (Fe<sub>90</sub>Co<sub>10</sub>)<sub>78</sub>Si<sub>12</sub>B<sub>10</sub>, to fabricate ME devices for both communication and sensing applications<sup>22,48–50</sup>.

For strain-mediated ME composites, it is critical to select piezoelectric materials with a high piezoelectric coefficient. Although perovskite ferroelectrics can exhibit high piezoelectric coefficients<sup>51</sup>, they are not compatible with CMOS technology owing to the requirement of epitaxial growth. Therefore, AlN and Sc-doped AlN are considered the premier candidates for use in ME composites<sup>51,52</sup>. Fabrication methods have also been developed to integrate ferroelectric lithium niobate, LiNbO<sub>3</sub>, on Si wafers via ion slicing and film transfer approach<sup>53,54</sup>, thus enabling LiNbO<sub>3</sub> deployment in future ME-based IoT devices.

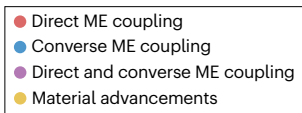
Doping galfenol (Fe<sub>80</sub>Ga<sub>20</sub>) films with boron or carbon causes a crystallographic phase transition from the body-centred cubic phase to an amorphous structure, leading to excellent soft magnetic properties (<2 Oe coercive field), high magnetostriction (78 ppm), near unity magnetomechanical coupling factor (0.84), and low ferromagnetic resonance linewidth in X-band (<20 Oe linewidth) in the body-centred cubic-amorphous phase boundary region<sup>14,36,55,56</sup>, making Fe<sub>1-x</sub>Ga<sub>x</sub> alloys the most promising magnetic materials for ME devices<sup>14,55–57</sup>. Novel growth approaches utilizing molecular beam epitaxial growth of Fe<sub>1-x</sub>Ga<sub>x</sub> films on PMN-PT have expanded the possible composition range for the disordered body-centred cubic (A<sub>2</sub>) phase space, achieving an ultra-high magnetostriction at a Ga concentration of  $x = 30\%$  with a diminishing stiffness, thus limiting their applications<sup>58</sup>. Underlayers such as NiFe, Cu, Cr, or Ti seed layer (<5 nm) before magnetic film deposition were demonstrated to promote soft magnetic properties in Fe-Ga alloys<sup>39</sup>.

Aside from the magnetomechanical properties and static magnetic behaviour, magnetic loss is a key property, particularly for RF ME NEMS. Magnetic loss can be understood by characterizing the ferromagnetic resonance linewidth and/or the Gilbert damping parameter<sup>60</sup>. Yttrium iron garnet (Y<sub>3</sub>Fe<sub>5</sub>O<sub>12</sub>, YIG) films are the pinnacle for low magnetic losses with an intrinsic magnetic damping parameter as low as approximately  $3 \times 10^{-5}$ , with the lowest reported magnetic damping parameter for the thin film regime at approximately  $5.2 \times 10^{-5}$  (refs. 61,62). This low magnetic damping enables long spin wave decay lengths of more than 100 μm (refs. 63,64). However, a key challenge for YIG integration is the lattice-matching requirement for epitaxy, specifically requiring growth on a Gd<sub>3</sub>Ga<sub>5</sub>O<sub>12</sub> (GGG) substrate, which is not back-end-of-line CMOS compatible<sup>65,66</sup>. Although the GGG substrate allows for heteroepitaxial growth of YIG films, the GGG substrate can serve as a source of contamination in sputtered YIG films<sup>67,68</sup>. Although liquid-phase epitaxy grown YIG films have shown minimal to no contamination from the GGG substrate, liquid-phase epitaxy is not as back end of line compatible as sputtering<sup>69</sup>. In 2022, a buffer layer of diamagnetic Y<sub>3</sub>Sc<sub>2.5</sub>Al<sub>2.5</sub>O<sub>12</sub> thin film on GGG enabled the growth of YIG films with off-axis sputtering with suppressed Gd-contamination to enable decent Gilbert damping at few-kelvin (K) temperatures<sup>70</sup>. Despite recent work suppressing Gd-contamination from the GGG substrate, there is a need for more investigation into the integration of YIG with CMOS-compatible substrates such as silicon. Ion-slicing has been successfully executed on YIG and other oxide films such as ferroelectric perovskites over the past 20 years (refs. 53,54,71,72). However, the integration of YIG film on a piezoelectric layer has not been demonstrated and this is probably a viable path forward for efficient ME-based IoT devices with high magnetoelectric coupling quality factor ( $Q_{ME}$ ).

## ME-based memory and logic

Many pathways are being explored to create low-power non-volatile memories within the context of next-generation computing. The push for ultra-low-power logic-in-memory devices builds from the ability of multiferroics to control magnetism with an electric field at room temperature (magnetoelectric control)<sup>33</sup>. The magnetoelectric switching of a magnetoresistive element can operate at or below 200 mV, with a pathway to get down to 100 mV (ref. 73). A combination of structural manipulation via lanthanum substitution and thickness scaling in multiferroic BFO helped to scale the switching energy density down to -10 μJ cm<sup>-2</sup> and provides a pathway to get to attojoule-class nonvolatile memories (1 aJ per memory bit or logic element), a leap in energy efficiency compared with the pJ per bit requirement for dynamic random-access memory-based technology<sup>73</sup>. However, the presence of polarization fatigue caused by the degradation of the interface between the CoFe ferromagnetic metal and the oxide BFO harkens back to work on ferroelectric memories, which also suffer from fatigue. To address these degradation issues, it is possible to replace the ferromagnetic CoFe with Sr<sub>2</sub>(Cr,Re)O<sub>6</sub>, a double perovskite ferrimagnet, which has proven to be successful if coupled to the BFO layer<sup>43</sup>. An alternative pathway is to eliminate the ferromagnetic layer and read out the magnon transport in the BFO (and its manipulation with an electric field) using the inverse spin Hall effect (statement based on study currently under review)<sup>74</sup>.

Logic-memory architectures<sup>32</sup> bring together the inverse Rashba-Edelstein effect (IREE)<sup>75,76</sup> and electric-field control of magnetism using multiferroic materials. The resulting magnetoelectric spin-orbit-coupled logic device (MESO)<sup>34</sup> uses the IREE effect to convert spin



## Applications of magnetoelectrics

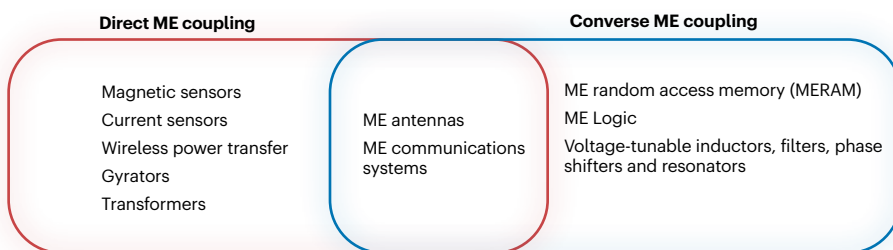


**Fig. 1 | Timeline of key contributions to ME materials and devices.** On the timeline, the seminal works are colour coded to exemplify whether they are material advancements (yellow), direct magnetoelectric (ME) coupling (blue), converse ME

coupling (red) or both direct and converse ME coupling (purple)<sup>2–31</sup>. Applications of direct and converse ME coupling mechanisms are summarized in the Venn diagram. VLF, very low frequency. WPT, wireless power transfer.

to charge (or voltage) and the multiferroic component to perform the opposite conversion of charge to spin<sup>24</sup>. These devices would be successful if an increase in the IREE voltage output from hundreds of microvolts ( $\mu\text{V}$ ) to hundreds of millivolts (mV) and a reduction in voltage requirement for the magnetoelectric component down to  $\sim 100$  mV (which is critical for obtaining an aJ per memory bit or logic element) are demonstrated<sup>24</sup>. Going to switching voltages below 100 mV in ferroelectric and multiferroic states is a challenging research opportunity, which requires the reduction of the coercive field either through pushing the BFO layer to a phase boundary or selecting another multiferroic material. Scaling down to 100 mV also necessitates low switching fields (for example, through careful tuning of the Landau double well barrier height) or that the switching behaviour scales well with reduced thickness. The ultrathin limits ( $< 20$  nm) are crucial and require further theoretical and/or experimental exploration.

The speed limit of the switching between ferroelectric and multiferroic seems to be linked to the acoustic phonon mode (that is the velocity of sound in the material, around  $3,000 \text{ m s}^{-1}$ ) tied to lattice deformation during polar state switching, indicating switching times on the order of tens of picoseconds. However, accessing such time-scales mandates rapid electronics (for example, sub-ten picosecond pulse generators, high-speed oscilloscopes), explaining limited measurements in this domain<sup>77</sup>. Lattice dynamics during dipolar switching requires extensive study. Such studies are needed to understand the switching dynamics of both multiferroics and ferroelectrics<sup>78</sup>.

Another aspect of importance in the ultrathin limit is the stability of the polar state. Such size effects have been extensively studied in classical ferroelectrics<sup>79</sup> that are characterized by a suppression of the order parameter as the thickness is scaled down. In BFO, the polar order parameter is suppressed below 4 nm (ref. 78). However, the stability of the individual order parameters, the coupling between them and electric field manipulation of this coupling below 10 nm are still to be studied.

Magnetoelectrics have also been proposed for ME random access memories: ultrathin ferroelectric or multiferroic layers can be used as the tunnel barrier of a magnetic tunnel junction to modify the magnetoresistance of the junction via interfacial spin polarization<sup>80–82</sup>. This approach is limited by the ferroelectric thickness because of the film polarization stability in the ultrathin limit. Alternatively, the magnetic tunnel junction can be directly grown on a bulk ferroelectric substrate<sup>83–85</sup>. Although the magnetoresistance can be tuned via rotating the free ferromagnetic layer, this approach is commercially nonviable owing to the use of bulk ferroelectric substrates.

## ME-based magnetometers

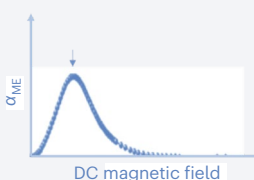
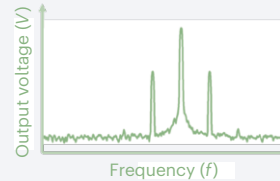
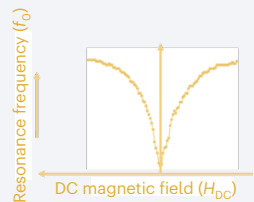
Magnetometers are widely used in biomagnetic sensing, navigation, magnetic anomaly detection, communications and so on<sup>86</sup>. Biomedical magnetometry is an application space that requires the detection of magnetic field signals in frequency ranges of 1–1,000 Hz and amplitudes of  $\sim 20$  fT to tens of pT to monitor brain, nerve, skeletal muscle, and heart functions<sup>87–90</sup>. As of the beginning of 2024, superconducting quantum interference device magnetometers are state-of-the-art in terms of high-sensitivity biomedical magnetometry.

A superconducting quantum interference device can detect magnetic signals in the single-digit fT range; however, the cryogenic cooling requirement drastically limits the overall form factor, power efficiency and applications<sup>91</sup>. Magnetoelectric magnetometers can operate at room temperatures with demonstrated detection of single-digit fT magnetic fields at kHz (C.D. et al., manuscript in preparation) and are, therefore, well suited to lower the cost, power consumption and form factor for biomedical magnetometry systems<sup>86</sup>. Although ME magnetometers are best-in-class for low-frequency magnetic field sensing, biocompatible implantable devices have yet to be demonstrated; polymer encapsulation may be a path towards in vivo demonstration.

There are three main schemes of magnetoelectric magnetometry: direct detection, frequency modulation and  $\Delta E$  effect (magnetic field-induced change in Young's modulus). The corresponding operating principle and noise spectral density (or magnetic noise, in units  $\text{T Hz}^{-0.5}$ ) for each scheme are reported in Table 1 (refs. 18, 23, 92–95). Direct detection relies on detecting alternating current (AC) magnetic fields via the direct ME effect – an AC magnetic field-induced alternating magnetostrictive strain translates to a stress variation in the piezoelectric layer. The relative change in electrical polarization can be monitored via an electrical voltage readout. The primary metric that indicates the promise of a direct detection ME magnetometer is the dependence of the ME voltage coefficient on the applied magnetic field. Typically, these ME magnetometers require a direct current (DC) magnetic bias field to push the sensor operation to the peak operating regime of the ME voltage coefficient in response to the applied magnetic field (Table 1). Reduced magnetic noise can be achieved through direct detection on the electromechanical resonance because the ME sensor output voltage is improved for magnetic signals that coincide with the mechanical resonance frequency (with demonstration of magnetic noise down to  $400 \text{ fT Hz}^{-0.5}$  (ref. 93) for MEMS ME sensors, and  $3 \text{ fT Hz}^{-0.5}$  for bulk ME sensors (C.D. et al., manuscript in preparation)). Additionally, operating the ME sensor in vacuum (for example, keeping the environment pressure below  $10^{-5}$  mbar) can lead to a further reduction of the noise (owing to less air damping) and, therefore, to an increase in  $Q_{\text{MR}}$  (ref. 96). Using these direct detection methods, on-resonant ME sensors have a limit of detection in the single-digit fT – pT regime. The resonance enhancement, however, comes at the cost of reduced bandwidth. Detecting low-frequency magnetic fields can be challenging because, below resonance and in the low frequency regime, the sensors suffer from  $1/f$  noise<sup>93,97</sup>. To circumvent operation at mechanical resonance while still maintaining the necessary sensitivity at lower frequencies, active frequency modulation, either magnetic or electrical<sup>98</sup>, as well as the  $\Delta E$  effect can be used (Table 1).

The frequency modulation approach presents two operation schemes: the magnetic and the electric frequency conversion. Magnetic frequency conversion exploits the nonlinearity of magnetostriction versus magnetic field. An advantage of magnetic modulation frequency conversion is that the sum of the modulation and signal frequencies can be selected to be equal to the mechanical resonance of the sensor; thus, resonant operation can be exploited for any arbitrary signal frequency<sup>97</sup>. The magnetic noise is, therefore, reduced because the resonance enhancement can be exploited<sup>99</sup>. For example, an ME

**Table 1 | ME magnetometer noise performance and operating schemes**

Sensing	Direct detection		Frequency modulation		$\Delta E$ effect	
Sub-approach	Bulk ME sensors	Thin-film ME sensors	Magnetic-driven frequency conversion	Electric-driven frequency conversion	Love wave acoustic mode	Bulk wave acoustic mode
Best-in-class reported noise spectral density	5 pT Hz <sup>-0.5</sup> @ f=1 Hz (ref. 92) 3 fT/Hz <sup>-0.5</sup> @ f=24 kHz (C.D. et al., manuscript in preparation)	10 nT Hz <sup>-0.5</sup> @ f<100 Hz (ref. 92) 400 fT Hz <sup>-0.5</sup> @ f=1 kHz (ref. 93)	60 pT Hz <sup>-0.5</sup> @ f=10 Hz (ref. 95)	10 nT Hz <sup>-0.5</sup> @ f=10 Hz (ref. 94)	250 pT Hz <sup>-0.5</sup> @ f=10 Hz (ref. 23)	300 pT @ quasi-DC (ref. 19)
Sensing mechanism						

For direct detection scheme, the performance is tied to the ME voltage coefficient ( $\alpha_{ME}$ ) as illustrated. The sensitivity of the magnetometer is optimized when the ME voltage is maximized; this can be accomplished by biasing the magnetometer with an external direct current (DC) magnetic field. With respect to the frequency modulation scheme, the sensitivity is enhanced through resonant operation at side bands. The example curve shows the upconversion of low-frequency magnetic signals to higher frequencies by frequency modulation for detection. The magnetometer can be operated at a sideband wherein there is a local maximum in the output voltage (V) versus frequency (f). The sensor will, thus, benefit from resonant enhancement. For the  $\Delta E$  effect sensors based on resonator nano-electromechanical systems, the device resonance frequency ( $f_0$ ) varies with changes in the elastic modulus of the magnetic material under an applied DC magnetic field. The resonance frequency can be monitored as shown in the illustration.

sensor based on FeCoSiB/AlN heterostructures showed a magnetic noise down to 60 pT Hz<sup>-0.5</sup> at 10 Hz (ref. 95). Electric frequency conversion relies on a piezoelectrically induced AC actuation of the sensor, which through the strain-mediated interface, results in an additional magnetic oscillation in the magnetostrictive component with side band generation<sup>97</sup>. An ME sensor based on an exchange-biased FeCoSiB stack showed a magnetic noise in the low nT Hz<sup>-0.5</sup> range<sup>94</sup>. The electric frequency conversion approach has a smaller form factor and lower power consumption than the magnetic modulation one because it does not require an external driving coil. For both approaches, ME sensors based on frequency modulation are less susceptible to the  $1/f$  noise – which dominates at lower frequencies – and, thus, have improved magnetic noise compared with the passive operation of the sensors<sup>100</sup>.

The  $\Delta E$  effect is the change in the Young's modulus,  $E$ , of a magnetic material, when a magnetic field is applied. This change provides additional magnetic field-induced magnetostrictive strain to the elastic Hookean strain<sup>101</sup>. Upon the application of an external magnetic field, the Young's modulus of an ME resonator changes because of the  $\Delta E$  effect and, therefore, a variation in the electromechanical resonance frequency and impedance is observed (Table 1). Self-biased NEMS magneto-electric sensors based on the  $\Delta E$  effect have been demonstrated in a FeGaB/AlN nano-plate resonator with a DC magnetic field detection limit down to 300 pT (ref. 19). Additionally, Love wave sensors based on the  $\Delta E$  effect have a magnetic field dependent phase change caused by the variations in the elastic properties of the magnetic film and, therefore, the wave speed<sup>23</sup>. Love wave sensors based on FeCoSiB demonstrated a magnetic noise of approximately 100 pT Hz<sup>-0.5</sup> over a 50-kHz bandwidth and a dynamic range of 120 dB (ref. 23). A magnetic noise of 28 pT Hz<sup>-0.5</sup> at 10 Hz was demonstrated for a  $\Delta E$  effect Love wave surface acoustic wave sensor based on an exchange-biased stack of FeCoSiB and Ni<sub>81</sub>Fe<sub>19</sub> coupled to an antiferromagnetic Mn<sub>80</sub>Ir<sub>20</sub> layer<sup>102</sup>. The exchange-biased stack with FeCoSiB coupled to an AFM layer was designed to eliminate domain walls and, therefore, the magnetic  $1/f$

noise was reduced by 8 dB compared with a comparable control device without an exchange bias material stack<sup>102</sup>. Existing devices enable the detection of magnetic fields at levels of approximately fT Hz<sup>-0.5</sup> at 24 kHz (C.D. et al., manuscript in preparation), showing great potential for sensing extremely weak magnetic signals.

## ME antennas

Being one of the largest components in electronic systems, antennas have so far been resistant to size miniaturization, leading to electronics with large size, weight, power and cost (SWaP-C). Conventional compact antennas operate at their electromagnetic resonance, leading to antenna sizes comparable to their electromagnetic wavelengths, in the order of centimetres at GHz frequencies. In addition, conventional antennas are based on electric currents that suffer from platform effects, leading to a high profile.

ME antennas are mechanical antennas based on layered ME piezoelectric–magnetostrictive heterostructures (Fig. 2). By applying an AC voltage on the piezoelectric layer, oscillating mechanical strain is induced and transferred to the magnetostrictive film. This electric-mechanical-magnetic energy transduction at the electromechanical resonance triggers AC magnetization oscillation in the magnetic layer, leading to magnetic dipole induced electromagnetic radiation (Fig. 2a). The ME antenna can transmit and receive electromagnetic waves with the same ME heterostructure. Operating at their electromechanical resonance, ultra-compact ME antennas have dimensions comparable to their mechanical or acoustic wavelength, which is five orders of magnitude smaller than the electromagnetic wavelength (Fig. 2b). At the same time, ME antennas are based on magnetic currents, instead of electric currents; thus, ME antennas are immune from the platform effect and exhibit enhanced radiation on a ground plane<sup>22,26,31,32,49</sup> (Fig. 2c).

In 2017, the first ME film bulk acoustic resonator (FBAR) antenna was experimentally demonstrated, marking a significant milestone: it operated at 2.53 GHz and showed an antenna gain of -18 dBi. The structure presented a FeGaB/AlN ME resonating disk with a

thickness of  $\sim 1 \mu\text{m}$  and a diameter of  $200 \mu\text{m}$  released but anchored on a  $0.5\text{-mm}$ -thick Si substrate<sup>22</sup>. Mounting a conventional dipole antenna on a ground plane, such as a metallic surface or human body can lead to a detuned antenna impedance and detrimental effects on the performance, as the ground plane can reflect, absorb, and scatter electromagnetic waves and cause destructive interference. ME antennas, however, use magnetic dipole for radiation and show ground plane immunity as the image dipole of the ME antenna on a ground plane is in-phase with the magnetic dipole itself. This ground plane immunity and a  $\sim 3 \text{ dB}$  gain enhancement on a ground plane have been observed for ME FBAR antennas<sup>27</sup>. ME antennas are ideally suited as conformal antennas for platform-independent deployments, such as in biomedical health monitoring<sup>103</sup>.

Despite the superior performance of ultra-high-frequency (UHF) FBAR ME antennas as conformal antennas over various ground plane platforms, they present physical fragility because they are released and suspended devices<sup>22</sup> (Fig. 3a). Solid-mounted resonator (SMR) ME antennas utilize acoustic Bragg reflectors to robustly support ME resonators and effectively confine acoustic energy, enabling comparable performance with  $24 \text{ dB}$  enhanced power handling compared with FBAR ME antennas<sup>31,49</sup> (Figs. 2d and 3b). The performance of the ME antenna can be further improved through an array topology: the simulated induced output voltage of the mechanically driven ME antenna can be tripled by using three ME resonators in series compared with a single resonator owing to nonlinear coupling<sup>26,104</sup>. Additionally, the bandwidth of the ME antenna can be larger through a resonator array with varying resonance frequencies (either through varying the thickness or the width of the resonator, depending on the targeted acoustic mode)<sup>104</sup> (Fig. 3c). These UHF ME antennas are self-biased and passive devices with much higher gains than similarly sized conventional antennas, making them ideal for portable and/or wearable IoT devices or biomedical implantable devices<sup>26</sup>.

VLF ME antennas (3–30 kHz) have been experimentally demonstrated and patented<sup>21,29,30</sup> (Fig. 3d). The VLF signals can penetrate deep into dense and lossy media, such as water, soil and rock. State-of-the-art VLF antennas have dimensions that are miles across and are too large to be implemented in underwater or underground environments. For base station VLF transmitters, these physically gigantic VLF antennas are still electrically small compared with their wavelength, have low radiation resistance and consume megawatts (MW) of power<sup>105</sup>. In 2020, experimental and theoretical results on ultra-compact ( $\sim 10 \times 1 \times 0.1 \text{ cm}^3$ ) ME mechanical antennas and ME communication systems have been demonstrated with distances over  $120 \text{ m}$  (ref. 30). The maximum transmission distance of a single mechanical antenna is still a few hundred metres within near-field range, restricting long-distance communication<sup>30</sup>. In 2022, a VLF ME 12-antenna array with a high converse magneto-electric coupling quality factor ( $Q_{\text{CME}} = 120$ ), greater than twice the typical value of 48, was demonstrated, showing an order of magnitude increase in radiation over a single ME antenna<sup>29,41</sup> (Fig. 3e). The compact ME antenna array could linearly enhance its radiation  $B$ -field strength from  $20 \text{ nT}$  for a single unit to  $210 \text{ nT}$  for a 12-element array. Both the radiation magnetic field intensity and the antenna efficiency were linearly boosted using a large number of arrays<sup>29</sup>.

High-Q VLF ME antennas have a very limited bandwidth, which can be overcome through a nonlinear antenna modulation scheme to potentially achieve a high data rate of  $2\text{--}10 \text{ kbps}$  without the use of a mixer. A data rate that is one order of magnitude higher than that of state-of-the-art VLF communication systems<sup>106</sup>. Combining the enhanced field strength via array deployment with high data rate via a nonlinear antenna modulation, VLF ME antenna arrays can realize ultra-compact mobile bi-directional VLF communication links between underwater and shore or between underwater and air across the air-water boundary<sup>29</sup>. VLF underwater and underground sensor networks can, thus, happen with the help of the earth-ionosphere waveguide. Up to  $5 \text{ m}$  under water, ME antenna arrays in seawater environments

## Characteristics of magnetolectric antennas

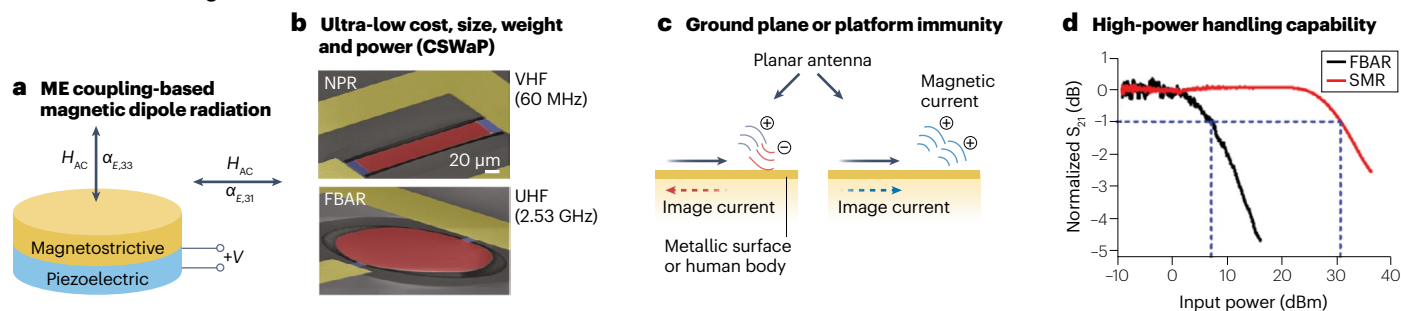


**Fig. 2 | Smart ME antenna characteristics.** **a**, Magnetolectric (ME) antenna piezoelectric–magnetostrictive composites. In the transmitting mode, an alternating current (AC) voltage is applied to the piezoelectric layer, generating a strain wave via piezoelectric effect. The strain wave induces the magnetostrictive film deformation and triggers the magnetization dynamics for AC magnetic field radiation ( $H_{\text{AC}}$ ). In the receiving mode, the magnetization in response to the radiofrequency (RF) magnetic fields from electromagnetic waves leads to magnetic film deformation owing to magnetostriction effect. The strain in magnetic film gives rise to the deformation of the piezoelectric layer and generates RF voltage output via inverse piezoelectric effect. The strain-mediated transverse ( $\alpha_{E,31}$ ) and longitudinal ( $\alpha_{E,33}$ ) ME coupling leads to in-plane and out-of-plane radiation magnetic field  $H_{\text{AC}}$ . **b**, Scanning electron microscopy (SEM) image of ME antenna at very-high-frequency (VHF) and ultra-high-frequency

(UHF) bands, showing ultra-low cost, size, weight, and power (CSWaP) feature of ME antennas. **c**, Illustration of ground plane or platform immunity of ME antennas. The out-of-phase imaging electric current of a conventional electrical antenna mounted on a metallic surface, ground or human body cancels the antenna radiation (left side), whereas ME antenna utilizes magnetic current for radiation and its in-phase imaging current contributes to  $3 \text{ dB}$  gain enhancement of ME antenna radiation (right side). **d**, Power handling test of the film bulk acoustic resonator (FBAR) and solid-mounted resonator (SMR) antennas. The FBAR antenna has a  $1 \text{ dB}$  compression point (P1dB) of  $7.1 \text{ dBm}$  whereas the P1dB of SMR antenna is  $30.4 \text{ dBm}$ , indicating that SMR antenna shows much better power handling capability. Panel **b** is reprinted from ref. 22, CC BY 4.0. Panel **c** is adapted with permission from ref. 27, IEEE. Panel **d** is reprinted from ref. 31, CC BY 4.0.

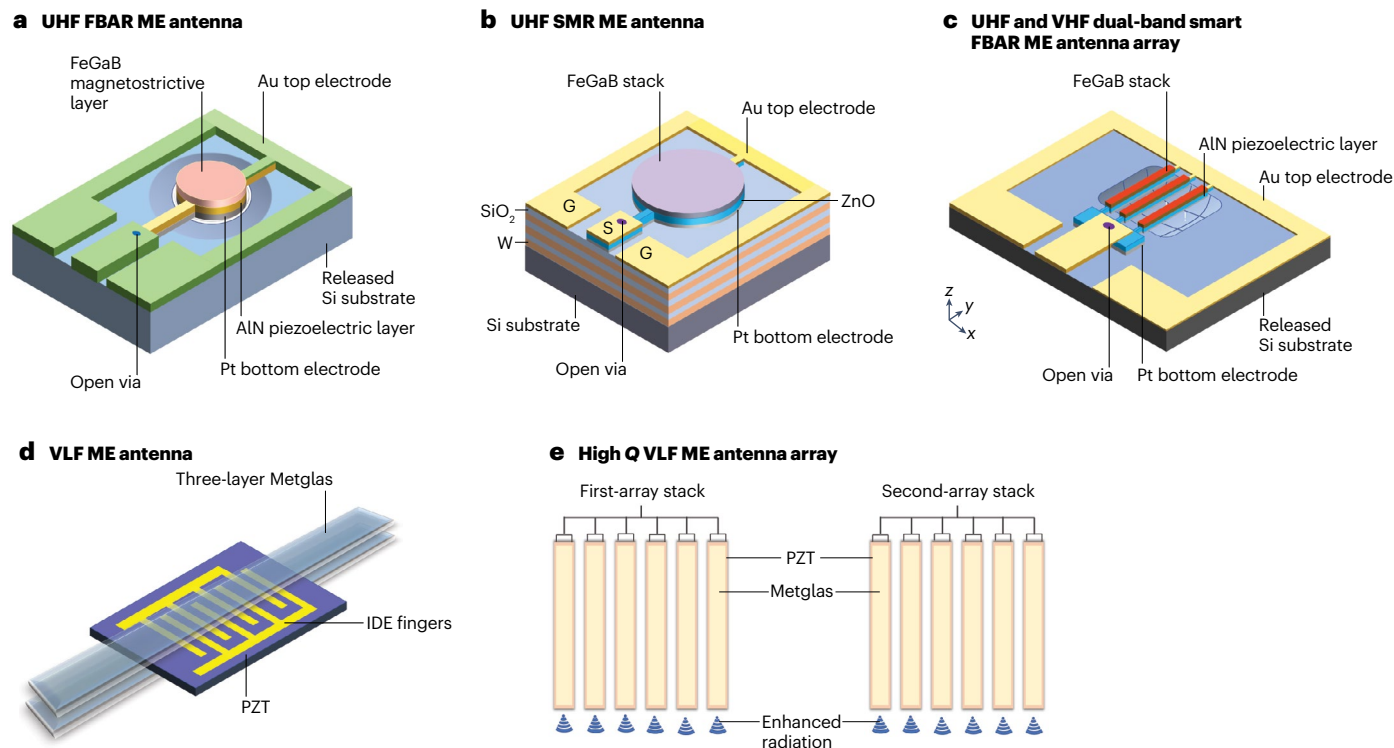


**Fig. 3 | UHF and VLF ME antenna architecture.** **a**, Magnetostrictive (ME) ultra-high-frequency (UHF) film bulk acoustic resonator (FBAR) antenna based on FeGaB/AlN resonator. The Si substrate below the resonator was released by XeF<sub>2</sub> vapour to form a free vibrating resonator with respect to anchors. **b**, ME solid-mounted resonator (SMR) antenna based on FeGaB/ZnO resonator on (SiO<sub>2</sub>/W)<sub>3</sub> acoustic Bragg reflectors. **c**, Very-high-frequency (VHF) and ultra-high-frequency (UHF) dual-band smart ME antenna for magnetic sensing and

wireless communication and power transfer. **d**, ME very-low-frequency (VLF) antenna based on PZT fibres sandwiched by three layers of Metglas on top and bottom. The deformation of PZT fibres is excited by interdigital electrodes (IDE). **e**, Quartz/Metglas VLF ME antenna array for underground and underwater communication. Panel **c** is adapted from ref. 26, CC BY 4.0. Panel **e** is adapted with permission from ref. 41, IEEE.

show similar transmission behaviours as in air, with no reflection at the seawater–air boundary<sup>29</sup>. As the equivalent dipole moment amplifies a thousand-fold, over a 30-m transmission distance at 24 kHz becomes achievable<sup>29</sup>. Compared with other mechanical antennas<sup>107</sup>, VLF ME antenna performance shows a magnetic noise of  $\sim 3$  pT Hz<sup>-0.5</sup> at 24 kHz and, thus, are extremely sensitive receivers (C.D. et al., manuscript in preparation). Overall, VLF ME antennas have the advantage of ultra-compact size, low power consumption,  $10^{-15}$  T magnetic field sensing,  $10\times$  enhanced data rates, and enhanced radiation strength and efficiency with array deployment compared with alternative mechanical antenna approaches.

## ME WPT

WPT enables versatility in applications wherein passive operation is desired, as in the case of IoT sensor nodes installed at locations with limited approachability or for invasive bioimplants. Layered ME heterostructures have been adopted and studied for WPT. In this case, the magnetostrictive material picks up the magnetic field in space and converts it to strain. The strain is then transferred to the piezoelectric layer through ME coupling, giving an electric voltage usable as a power supply<sup>108–110</sup>.

Besides WPT, ME antennas can harvest energy from mechanical vibrations and magnetic fields<sup>108–110</sup>. The magnetic field-based energy

harvesting devices directly pick up the magnetic fields in space either in stray form or as the transmitted signal. The WPT efficiency of a ME receiver can reach more than 80% (refs. 111,112), which is comparable to or higher than the resonant coil-to-coil inductive WPT link. At large distances, ME receivers can have efficiencies one order of magnitude higher than the ones obtainable by resonant coil-to-coil WPT links, making ME antennas competitive candidates for large-scale and long-distance WPT networks<sup>113</sup>.

Taking advantage of their ultra-compact sizes and high efficiency for data transmission and WPT, ME antennas have great potential for bioimplant applications, especially considering the strict size limitations and high energy absorption in tissues at higher frequency<sup>114</sup>. In this direction, engineering novel materials for device flexibility and biocompatibility<sup>115,116</sup>, and developing system-level bioimplants for magnetic sensing and stimulation<sup>117</sup> have become paramount. For example, NEMS smart ME antennas can perform WPT and magnetic field sensing simultaneously<sup>26</sup>. The achieved figure of merit for WPT is one to two orders higher than that of miniaturized micro-coils with a magnetic field limit of detection of 300–500 pT between 100 and 1,500 Hz. In another example, a system-level ME bioimplant with an output power of 1.17 mW was obtained under a 6 W transmitter power at an operating distance of 30 mm and was used to produce a 3 Hz stimulation in a rat model<sup>103</sup>. The subsequent works on ME bioimplants



combined data communication and WPT and optimized the modulation schemes for a backscattered communication system<sup>118,119</sup>. These ME antennas with excellent performance on data communication and WPT enable ultra-compact passive IoT devices for simultaneous wireless information and power transfer operation in a single device, as demonstrated they exploit distinct acoustic resonance modes, enabling simultaneous magnetic field sensing, data communication, and WPT<sup>26</sup>.

## MEs for power, RF and microwave electronics

In the realm of power, RF and microwave electronics, tunable and nonreciprocal components with compact size and superior power efficiency are in high demand. In this section, we focus on magnetoelectric and magnetoacoustic devices and systems that enable tunability and nonreciprocity and exhibit promising compactness, power efficiency and versatility.

### ME-tunable components

The demand for tunability in RF devices, driven by size reduction, cost-effectiveness and versatility requirements has led to the exploration of methods such as CMOS switches and varactors, M/NEMS switches and varactors, ferroelectric varactors, and magnetics<sup>120</sup>. However, these approaches are slow, bulky and power-hungry and often introduce discrete tunable states, structural fragility. ME materials exhibit electric field and magnetic field control of high permeability and permittivity, ferromagnetic resonance (FMR), and non-uniform spin waves, which can be harnessed for tunable power, RF and microwave components, including inductors, filters, phase shifters and resonators<sup>120</sup>. The strain generated through piezoelectric or electrostrictive effects induces an effective magnetic field, altering magnetic properties and device performance<sup>16,17</sup>.

Tunable permeability or Faraday rotation<sup>121</sup> in ferrites are leveraged to achieve phase shifts through transmission line<sup>122–127</sup> or waveguide structures<sup>128</sup>. The Polder tensor, linked to the frequency and magnetic field, dictates the phase shift, thus enabling tunability via piezoelectric–electrostrictive materials. This capability was demonstrated for phase shifters based on a partially biased ferrite YIG, and tunable phase shifters using a YIG/PMN-PT ME laminate<sup>124</sup> (Fig. 4a). These examples underscore the potential for ME materials as low-cost, power-efficient, tunable components.

Inductors are ubiquitous circuit elements. To enhance the performance of the inductors and reduce their size, high-permeability materials such as NiFe permalloy<sup>129</sup>, NiZn–ferrite<sup>130</sup>, FeCoCu (ref. 131) and FeGaB (refs. 132,133) are used as magnetic cores. Magnetic or insulator laminated cores<sup>133–135</sup> are used to mitigate eddy currents. However, these inductors are typically not tunable or are tuned via an applied magnetic field, which is not a scalable approach. ME inductors with a magnetic/ferroelectric ME heterostructure core have been demonstrated with voltage-tunable inductance, increased inductor quality factor ( $Q_L$ ), and reduced eddy current loss<sup>35,136–138</sup>. Voltage-tunable inductors composed of PZT and Metglas demonstrated a remarkable 450% inductance tunability at 1 kHz (ref. 138), albeit with restricted operating frequencies owing to the large eddy currents in the Metglas. FeGaB/Al<sub>2</sub>O<sub>3</sub>/PMN-PT composites yield gigahertz-range inductors with a maximum  $Q_L$  of 32.7% and 191% inductance tunability at 1.5 GHz (ref. 136) (Fig. 4b).

Tunable bandpass or bandstop filters are widely used for frequency selectivity in signal processing. Magnetic material-based bandstop filters leverage the FMR absorption for notch frequency characteristics,

using ferrite<sup>139–143</sup> or FeGaB (ref. 144). Piezoelectric–electrostrictive materials bonded to magnetic layers enable voltage-based frequency tuning. YIG/PZT heterostructures produced a bandstop filter with 15 MHz tuning at –50 dB in-band rejection<sup>145</sup>. ME coupling facilitates voltage-tunable bandpass filters via magnetostatic surface wave transmission in ferrites. The magnetic field-dependent dispersion relation of magnetostatic surface waves permits direct or strain-induced magnetic field tuning<sup>146</sup>. For example, electrically and magnetically tunable ME bandpass filters were demonstrated using NiZn ferrite and PMN-PT slab<sup>147</sup> (Fig. 4c). Additionally, ME-based mechanical resonance led to tunable frequency selectivity in free-standing FeGaB/Al<sub>2</sub>O<sub>3</sub> structures<sup>148</sup> (Fig. 4d).

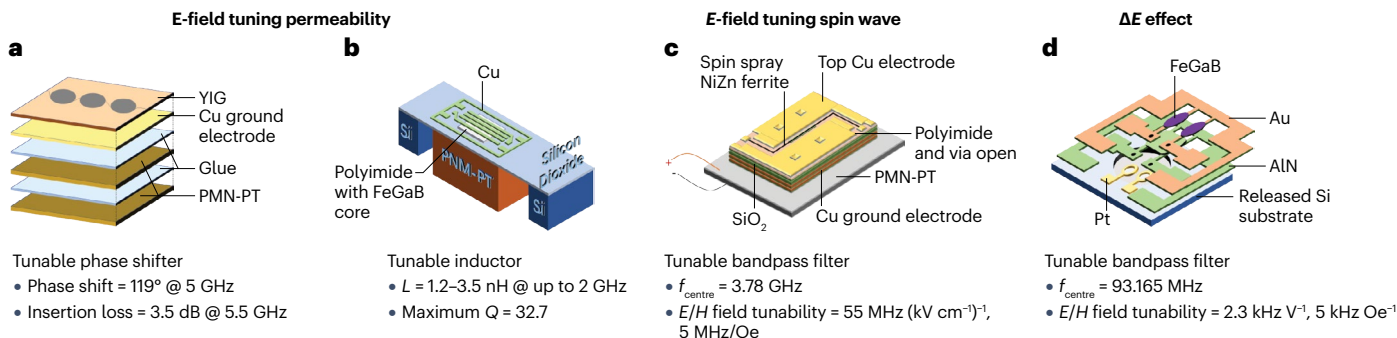
Tunable ME resonators are crucial for studying the fundamental electromagnetic coupling in tunable ME devices such as filters, phase shifters, and inductors, which are based on magnetic/ferroelectric or magnetic/piezoelectric multiferroic heterostructures<sup>149</sup>. Compared with conventional tunable resonators by magnetic field from magnetic cores, these heterostructures with strong converse ME coupling enable effective voltage control of magnetism, providing great opportunities for compact, lightweight, and power-efficient voltage-tunable RF and microwave signal processing devices<sup>150</sup>. The ME resonators also have competitive tuning range, tuning speed, power handling, linearity, and cost. One notable milestone of the ME resonators is the realization of a novel FeGaB/PZN-PT heterostructures<sup>17</sup>, which exhibit a record high electrostatically tunable FMR frequency range of 5.82 GHz with a ratio between  $f_{\max}$  and  $f_{\min}$  of 4.3, and a giant electrostatically induced magnetic anisotropy field of 750 Oe at both DC and microwave frequencies. The giant frequency tunability makes these FeGaB/PZN-PT multiferroic heterostructures attractive for voltage-tunable microwave ME devices.

### Nonreciprocal magnetoacoustic RF devices

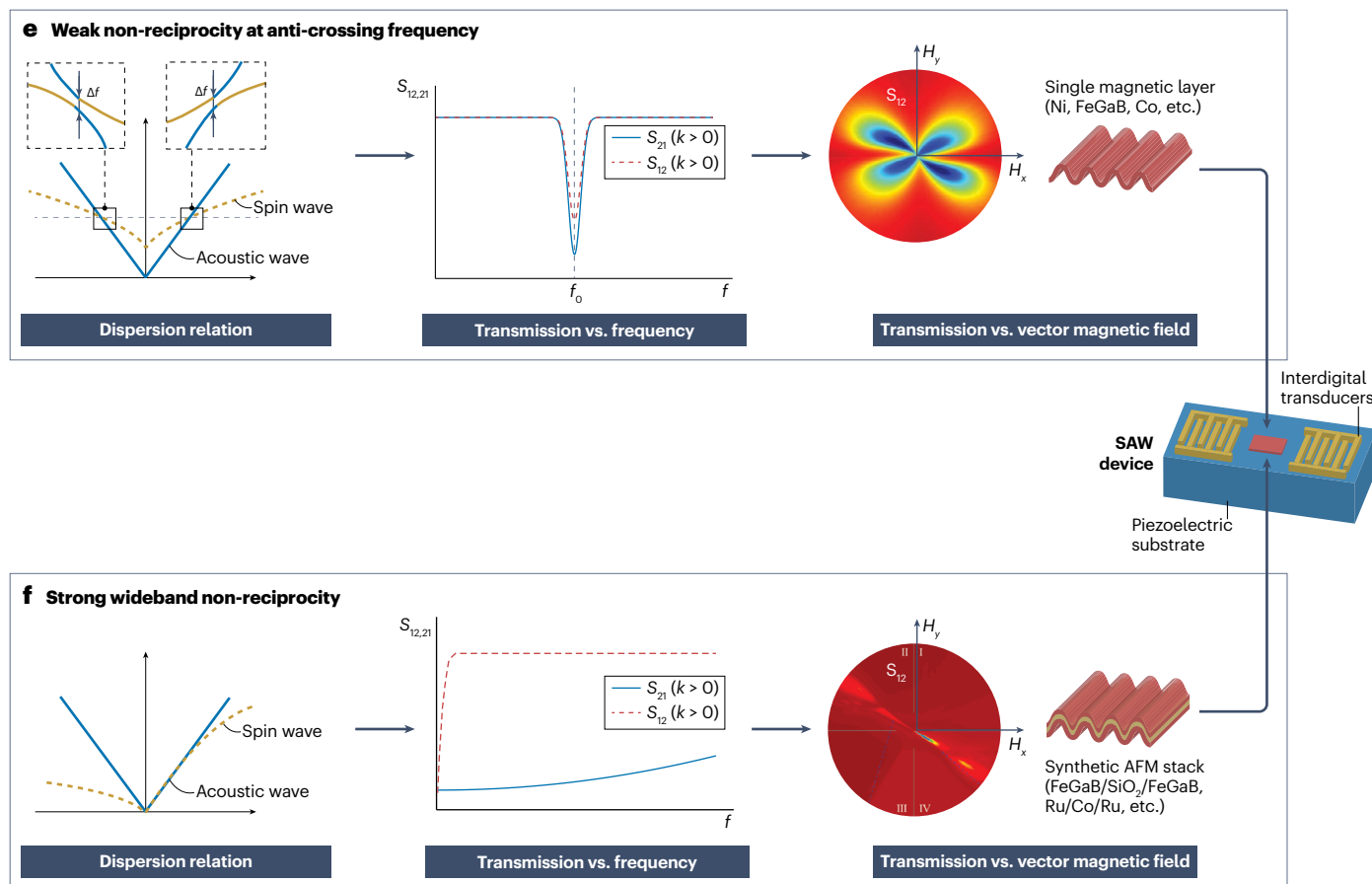
Integrated nonreciprocal components, such as isolators and circulators, have revolutionized wireless communication and sensing methods<sup>151–153</sup>. Isolators serve as safeguards, preventing back reflections from affecting on-chip high-power amplifiers<sup>151–153</sup>. Meanwhile, integrated circulators, in combination with self-interference cancellation techniques, pave the way for in-band full-duplex operations in upcoming wireless systems and networks<sup>151–153</sup>. However, the integration of full-duplex transceivers based on these integrated CMOS circulators and self-interference cancelers primarily cater to high-power wireless applications and involve considerable DC power consumption ranging from tens to hundreds of milliwatts. The current iterations of CMOS circulators<sup>151–153</sup> built upon transistor modulation exhibit high power usage (40–200 mW), rendering them less suitable for low-power applications. Additionally, existing integrated CMOS nonreciprocal components encounter bandwidth limitations owing to their dependence on resonant ring structures<sup>151–153</sup>, leading to compromises in power handling when prioritizing wider bandwidths<sup>154,155</sup>. Innovative integrated nonreciprocal technology featuring superior power efficiency, linearity and isolation is needed to enable low-power applications within the emerging landscape of IoT.

Nonreciprocal magnetoacoustics through the coupling of surface acoustic wave with nonreciprocal spin waves emerges as a novel approach for integrated nonreciprocal RF devices<sup>156–160</sup>. The synergy between surface acoustic waves and spin waves results in substantial nonreciprocity accompanied by remarkable power efficiency. The hybridization lays the groundwork for on-chip integrated nonreciprocal magnetoacoustic RF components that seamlessly align with CMOS

## Magnetoelastic tunable RF/microwave components



## Efficient non-reciprocal magnetoacoustic isolator, phase shifter or circulator



compatibility, ideally suited for both low-power and wideband full-duplex wireless radio systems. The integrated systems hold immense potential for secure communications in the future of IoT, smart cities, smart grids and industrial automation. Notably, these magnetoacoustic devices bring together the functionalities of RF circulators and surface acoustic wave filters, streamlining systems, and radio attributes such as size, cost, complexity and overall efficiency.

The origin of the nonreciprocity of the hybrid magnetoacoustic devices lies in the interplay between surface acoustic waves and spin waves, leading to the emergence of two distinct hybrid magnetoelastic waves through the anti-crossing of magnons and phonons<sup>156</sup>.

Empirical evidence supporting nonreciprocal transmission in surface acoustic wave devices with various single magnetic film layers, such as FeGaB, Ni and Co<sup>37</sup>, underpins this principle. However, the strength and operational bandwidth of this transmission remains limited (Fig. 4e).

Ongoing research strives to increase both the coupling strength and bandwidth through magnetoelastic interactions between nonreciprocal spin waves and surface acoustic waves<sup>157–160</sup>. One such demonstration of nonreciprocity involved coupling surface acoustic waves to a perpendicular magnetic anisotropy stack made of Ta/Co<sub>20</sub>Fe<sub>60</sub>B<sub>20</sub>/MgO/Al<sub>2</sub>O<sub>3</sub> (ref. 161) with interfacial Dzyaloshinskii–Moriya interaction<sup>162</sup>. The chirality of rotational lattice deformation coupled with

**Fig. 4 | Magnetolectric tunable devices for RF, microwave and power electronics and efficient nonreciprocal magnetoacoustic isolator, phase shifter or circulator.** **a**, State-of-the-art tunable phase shifter<sup>125</sup> utilizing electric ( $E$ )-field tuning permeability in yttrium iron garnet (YIG)/Pb(Mg<sub>1/3</sub>Nb<sub>2/3</sub>)O<sub>3</sub>-PbTiO<sub>3</sub> (PMN-PT) heterostructure. It achieves a phase shift of 119° at 5 GHz and a low insertion loss of 3.5 dB at 5.5 GHz. **b**, State-of-the-art tunable inductor<sup>136</sup> utilizing  $E$ -field tuning permeability. Polyimide with FeGaB is used as a magnetic core. The permeability of FeGaB can be tuned by applying voltage on PMN-PT or a bias magnetic field. It achieves an inductance of 1.2–3.5 nH and a maximum inductor quality factor ( $Q_i$ ) of 32.7. **c**, State-of-the-art tunable phase shifter<sup>147</sup> utilizing  $E$ -field tuning spin wave. The dispersion relation of spin wave in NiZn ferrite tuned by an applied voltage on PMN-PT or a bias magnetic field allows bandpass transmission centred at 3.78 GHz, with an  $E$ -field tunability of 55 MHz (kV cm<sup>-1</sup>)<sup>-1</sup> and a magnetic ( $H$ )-field tunability of 5 MHz Oe<sup>-1</sup>. **d**, State-of-the-art tunable bandpass filter<sup>148</sup> utilizing  $\Delta E$  effect. The applied voltage on the AlN piezoelectric layer or an applied bias magnetic field leads to the Young's modulus change of the FeGaB magnetostrictive layer. The Young's modulus change allows for bandpass transmission with an  $E$ -field tunability of 2.3 kHz V<sup>-1</sup> and a  $H$ -field tunability of 5 kHz Oe<sup>-1</sup>. **e**, Dispersive relation (left), transmission versus frequency (middle) and transmission versus vector magnetic field (right) of acoustic-driven spin resonance<sup>39,166</sup>. Acoustic-driven spin resonance shows

strong absorption but weak nonreciprocity at the anti-crossing frequency of the spin wave and acoustic wave modes. The corresponding devices incorporate single magnetic layers (Ni, FeGaB, Co, etc.) between interdigital transducers (IDTs) on the piezoelectric substrate, which can be used to efficiently excite quantum defects. **f**, Dispersive relation (left), transmission versus frequency (middle) and transmission versus vector magnetic field (right) of wideband nonreciprocal transmission<sup>25,166</sup>. Wideband nonreciprocity leverages the strong coupling between surface acoustic wave (SAW) and non-reciprocal spin wave in synthetic antiferromagnetic (AFM) stack (FeGaB/SiO<sub>2</sub>/FeGaB, Ru/Co/Ru, etc.), which is used for nonreciprocal isolators, phase shifters or circulators. Panel **a** is adapted with permission from ref. 125, IEEE. Panel **b** is adapted with permission from ref. 136, IEEE. Panel **c** is adapted with permission from ref. 147, IEEE. Panel **d** is adapted with permission from ref. 148, IEEE. In panel **e**, dispersive relation and transmission versus frequency graphs are reprinted with permission from ref. 166, APS, whereas transmission versus magnetic field vector graph is adapted with permission from ref. 39, AAAS. In panel **f**, dispersive relation and transmission versus frequency graphs are reprinted with permission from ref. 166, APS, whereas transmission versus magnetic field vector graph is modified from ref. 25, the authors, some rights reserved; exclusive licensee: AAAS. Distributed under a CC BY-NC 4.0 license.

magnetization, through magnetic anisotropies, induces pronounced nonreciprocal attenuation in surface acoustic waves, which can enable adaptable acoustic rectifiers, isolators and filters. In contrast to the confined Dzyaloshinskii–Moriya interaction-induced nonreciprocal band (10–100 MHz)<sup>163</sup>, Ruderman–Kittel–Kasuya–Yosida antiferromagnetic exchange<sup>164</sup> offers a wider nonreciprocal transmission band characterized by substantial isolation strength (Fig. 4f). This broader bandwidth response provides a pathway to versatile wideband nonreciprocal RF isolators, circulators, and phase shifters<sup>165,166</sup>. Experimental validation of this concept entails an antiferromagnetically coupled stack (FeGaB/Al<sub>2</sub>O<sub>3</sub>/FeGaB) situated between two interdigitated transducers on a lithium niobate substrate<sup>25,28</sup>.

## Emerging systems

Here we discuss the prospect and promise of emerging systems that should be further explored to improve the performance of magneto-electric materials and N/MEMS for wireless communication, magnetic sensing and quantum technologies relevant to IoT applications.

### Strong magnon–phonon coupling for energy-efficient transduction

Magnons and phonons are integral quasiparticles in the realm of solid-state physics. Magnons, the result of collective electron spin wave excitation, hold immense potential for applications in advanced information processing, communication and sensing. Their attributes, including tunable frequencies through magnetic fields, rapid operation, and extended transduction distances, stem from their high spin density and magnetic dipolar coupling<sup>38</sup>. Phonons, which denote collections of acoustic vibrations, excel as carriers of coherent and quantum information owing to their long lifetimes within solid-state platforms. The small wavelengths associated with acoustic waves make phonons particularly suitable for on-chip hybrid quantum systems<sup>167</sup>, with their frequencies conveniently adjustable through geometric manipulation. Coherent magnon–phonon coupling is a critical mechanism for seamless information transfer between magnon and phonon excitations<sup>168</sup>. These fundamental quasiparticles have a pivotal role in bridging various

other quantum information carriers. The coupling not only holds the promise of revolutionizing information technologies but also sparks interdisciplinary investigations into hybrid multi-physical cavities such as cavity optomechanics, optomagnonics, and magnomechanics<sup>169,170</sup>. A central aspect of strong magnon–phonon coupling, identified by anti-crossings in magnon and phonon dispersion relations, gives rise to hybrid magnetoacoustic modes termed magnon polarons. The strength of this coupling is quantified by equation (2):

$$C = \frac{g^2}{\kappa_M \kappa_P} = \frac{(\Delta f)^2}{4\kappa_M \kappa_P} \quad (2)$$

where  $g$  is the coupling strength of magnons and phonons and  $\Delta f$  is the mode-splitting frequency gap.  $\kappa_M$  and  $\kappa_P$  are the loss rates of the magnon and phonon modes, respectively<sup>157</sup>.

Recent research has focused on robust magnon–phonon coupling with improved acoustic resonance quality factor ( $Q_{\text{acoustic}}$ ) and spin resonance quality factor ( $Q_{\text{spin}}$ ), coupling strength ( $g$ ) and cooperativity ( $C$ ). This shift is driven by its potential contributions to magnon spintronics, spin caloritronics, and emerging phenomena such as the spin Seebeck effect, spin pumping, magnon–phonon conversion, and thermal Hall effect<sup>171,172</sup>. To enhance  $Q_{\text{acoustic}}$ ,  $Q_{\text{spin}}$ ,  $g$  and  $C$ , researchers are adopting innovative design methodologies. Strategies include reducing energy dissipation, localizing energy in specific coupling regions, and enhancing magnetoelastic coupling. Notable examples include creating Ni nanomagnets on Si substrates to achieve strong coupling using ultrafast pump-probe techniques<sup>173</sup> and leveraging perpendicular standing acoustic waves in GGG substrates to enhance coupling with magnons in low-loss YIG films<sup>174</sup>. In 2020, a galphenol nanograting with a high magnetoelastic coupling constant was introduced, leading to enhanced cooperativity<sup>175,176</sup>. Techniques such as Gaussian focusing interdigitated transducers in surface acoustic wave devices and Bragg reflectors for magnetoacoustic systems further enhance the coupling<sup>177–179</sup>. A strong magnon–phonon coupling in bulk YIG/AlN ME resonators, demonstrated in 2022, revealed insights into radiation efficiency

## Glossary

### **$\Delta E$ effect**

The change in the Young's modulus  $E$  of a magnetic material caused by an applied magnetic field, which adds additional magnetic field-induced magnetostrictive strain to the elastic Hookean strain.

### **Acoustic resonance quality factor**

The frequency-to-bandwidth ratio of acoustic resonance.

### **Converse magnetoelectric coupling**

The control of the magnetization oscillation in a material through an applied electric field. The strength of the converse ME effect for isothermal processes is described by the following equation:  $\alpha_{\text{Converse}} = \mu_0 ((\partial M / \partial E))_{T, H}$  where  $M$  is magnetization,  $H$  is magnetic field,  $E$  is electric field and  $T$  is temperature.

### **Converse magnetoelectric coupling quality factor**

Refers to the frequency-to-bandwidth ratio of the converse magnetoelectric coupling coefficient.

### **Direct detection**

Refers to magnetic field detection which is sensed via strain-induced magnetoelectric voltage.

### **Direct magnetoelectric coupling**

The control of the switching in the electric polarization of a material through an applied magnetic field. The strength of the direct ME effect for isothermal processes is described by the following equation:  $\alpha_{\text{Direct}} = (\partial P / \partial H)_{T, E}$ , where  $P$  is defined as polarization,  $H$  is magnetic field,  $E$  is electric field and  $T$  is temperature.

### **Electromechanical resonance**

Occurs in a piezoelectric micro-electrical-mechanical-system resonator or actuator when the frequency of the electrical signal matches with the natural mechanical resonant frequency of the device. At this resonant frequency, there is highly efficient transduction between electrical energy and mechanical motion, leading to an enhanced mechanical vibration amplitude.

### **Electrostrictive**

Describes the property of shape change under the application of an electric field in electrical non-conductors or dielectrics.

### **Ferrimagnetism**

A variant of magnetism whereby magnetic moments in a material are antiparallel. Unlike antiferromagnetism, the antiparallel moments have different magnitudes and, therefore, do not cancel each other out. The result is a spontaneous, net magnetization.

### **Ferroelasticity**

The property of those materials that exhibit spontaneous strains, specifically two stable strain states that have a hysteretic response to external force.

### **Ferroelectricity**

The property of certain dielectric materials that are characterized by a spontaneous electrical polarization even after the removal of the applied electric field. The orientation of their dipole moment can be altered by the application of an electric field. Electric dipoles and ferroelectricity violate spatial inversion symmetry.

### **Ferromagnetism**

The property of those materials wherein neighbouring magnetic moments align parallel to each other, resulting in a spontaneous macroscopic magnetization even in the absence of an external magnetic field.

### **Ferrotoroidicity**

The spontaneous long-range order of microscopic toroidal moments. Materials that show this property simultaneously break time-reversal and space-inversion symmetries without developing ferromagnetism or ferroelectricity.

### **Frequency modulation**

Enables conversion of low-frequency magnetic fields via piezoelectric actuation or external AC magnetic field modulation, thus allowing the magnetoelectric magnetometer to overcome  $1/f$  noise.

### **Inductor quality factor**

The ratio of inductive reactance to resistance at a given frequency. This parameter is used to evaluate the efficiency of storing and releasing energy and energy loss of an inductor.

### **Interfacial coupling coefficient**

Describes the quality of the interface between the magnetic and the piezoelectric components of a ME laminate. An interfacial coupling coefficient equal to 1 represents a perfectly bonded interface between the magnetic material and the piezoelectric phase, thus ensuring a perfect coupling between the two components and the possibility of transferring strain without appreciable losses.

### **Inverse Rashba–Edelstein effect**

Enables spin-to-charge conversion in systems with large Rashba spin splitting.

### **Longitudinal–longitudinal (L–L) mode**

Defined as the ME coupling between a longitudinal magnetization and a longitudinal polarization.

### **Magnetoelectric control**

Enables manipulation of the magnetic state via applied voltage in the device.

### **Magnetoelectric coupling quality factor**

The frequency-to-bandwidth ratio of magnetoelectric coupling coefficient.

### **Magnetoelectric materials**

(ME). Materials, either single phase or a composite, that possess both ferromagnetic and ferroelectric order. This definition is often expanded to include non-primary order parameters, such as ferrimagnetic or antiferromagnetic order.

### **Magnon spintronics**

A fascinating area of research that delves into structures, devices and circuits leveraging spin currents carried by magnons, offering exciting possibilities for energy-efficient computing and novel device architectures.

### **Magnon–phonon coupling**

Refers to the conversion between magnons (quanta of coherence procession of magnetic moments) and phonons (quanta of lattice vibration in a crystal).

### **Mechanical resonance quality factor**

Defined as the resonant frequency-to-bandwidth ratio of the mechanical resonator.

### **Multiferroic materials**

Materials with multiple primary ferroic properties. The primary ferroic properties include (1) ferromagnetism, (2) antiferromagnetism, (3) ferrimagnetism, (4) ferroelectricity, (5) antiferroelectricity, (6) ferroelasticity and (7) ferrotoroidicity.

### **Noise spectral density**

The magnetometer performance in units of  $\text{T}\cdot\text{Hz}^{-0.5}$ .

## Glossary (continued)

### Piezoelectric–magnetostrictive laminate composites

Heterogeneously integrated or monolithically integrated heterostructures that are composed of a bilayer film of a material with magnetic order and another with piezoelectric–ferroelectric order. The interface of this bilayer heterostructure strain couples the two materials.

### Platform effects

Refer to the detuned impedance or degraded radiation performance of an antenna when mounted on a ground plane platform such as human body.

### Quantum transduction

Refers to the coherent exchange of information between quantum systems without compromising quantum coherence.

### Spin caloritronics

A field that explores the interaction between spin (a quantum property of particles) and heat currents in materials.

### Spin pumping

The dynamic generation of pure spin current through the coherent precession of magnetic moments.

### Spin resonance quality factor

The frequency-to-bandwidth ratio of spin resonance.

### Spin Seebeck Effect

Refers to the generation of a spin current (electric potential) owing to a heat current (temperature gradient) within a magnetic material.

### Thermal Hall effect

Happens when a temperature gradient causes mobile charge carriers (usually electrons) to flow from the warmer end to the cooler end.

### Varactors

Semiconductor devices whose junction capacitance can be tuned by applying voltage.

enhancement with two split magnetoelastic radiation modes<sup>180</sup>. In the strong coupling region, the radiation efficiency can be enhanced by over two orders of magnitude with a maximum value of around 3.5% (ref. 180). This coupling can also significantly boost radiation efficiency in ME antennas, offering the potential for highly efficient IoT applications.

Key design parameters for robust magnon–phonon coupling are piezoelectric materials with high electromechanical coupling efficiency and magnetostrictive materials with low loss and high magnetostriction. The potential of ion slicing to create high-quality released YIG films for FBAR and SMR antennas, enhancing radiation efficiency, is also evident<sup>72,181,182</sup>. Additionally, the replacement of AlN with AlScN having six times enhanced piezoelectric constant<sup>183</sup> or use of materials with higher magnetostriction constants such as boron or carbon doped FeGa and FeCo alloys<sup>56,184,185</sup>, spinel NiZnAl–ferrite<sup>186</sup> and magnesium aluminum ferrite oxide MgAl<sub>0.5</sub>Fe<sub>1.5</sub>O<sub>4</sub> (ref. 187) holds promise for further enhanced coupling. These advances can enable highly efficient ultra-compact ME antennas with high radiation efficiency, ME sensors and magnon–phonon quantum transduction devices.

### ADFMR for efficient control of quantum defects

Quantum spin defects, such as nitrogen-vacancy centres in diamonds, are captivating owing to their multifaceted potential in quantum technologies: quantum sensing, quantum computing, quantum communication networks<sup>188–190</sup> and nanoscale magnetic biological sensing<sup>191–193</sup>. The spin states of nitrogen-vacancy centres can be optically detected and manipulated and are sensitive to nearby magnetic fields, enabling them to function as magnon probes<sup>194</sup> and potential transducers for converting GHz qubit excitations to optical photons<sup>195</sup>. Acoustic-driven ferromagnetic resonance through magnetoelectric bulk acoustic wave or surface acoustic wave resonators is an intriguing avenue for nitrogen-vacancy centre manipulation. Its energy efficiency and compatibility with on-chip integration hold promise for quantum communication, quantum sensing, and quantum information science. Electric control over nitrogen-vacancy centres using ME coupling within CoFeB/PMN-PT bulk acoustic wave resonators has been demonstrated<sup>40</sup>. Applying an external voltage to PMN-PT induced lattice strain in the CoFeB film, altering its magnetic anisotropy,

nitrogen-vacancy electron spin resonance and the nitrogen-vacancy centre relaxation rate.

ADFMR has emerged as an efficient approach for localized voltage control of nitrogen-vacancy centres with comparable Rabi frequencies to microwave excitation while consuming far less power<sup>196,197</sup>. A thin Ni or Co film between interdigital transducers was used for nitrogen-vacancy centre excitation, exhibiting power absorption symmetry peaking at  $\phi = 45^\circ$  (ref. 39). At 1,429 MHz, distinct nitrogen-vacancy photoluminescence emerged, aligned with nitrogen-vacancy centre's excited state resonance frequency. Cobalt–nitrogen vacancy coupling was notably stronger than nickel, resulting in comparable photoluminescence change with significantly lower electric absorption power. To bolster magnetic biosensing and improve energy efficiency of information transfer for quantum communication, coupling acoustic and spin waves effectively via surface acoustic wave resonators is essential. To reach this objective low-damping, magnetostrictive materials, CMOS-compatible piezoelectric materials, and improved interdigital transducer electrode design are required.

### VLF ME antenna arrays for underwater and underground communications

Underwater communications are pivotal for various oceanic activities, encompassing scientific, environmental, commercial, and military ventures. However, achieving high-speed, high-volume underwater wireless communications remains challenging owing to factors such as multi-path propagation, limited bandwidth and rapid signal attenuation<sup>198</sup>, especially over extended distances. Acoustic waves are predominantly used for underwater communications because they attenuate over a longer decay length in seawater than radio waves. However, acoustic signals suffer from the water–air communication barrier and have other limitations, such as low data rates, communication delays and high energy consumption<sup>30</sup>. VLF wireless communications between underwater and shore or air have been one-directional only from shore to underwater. The large VLF antenna sizes make mobile underwater VLF transmitters impractical. This prevents submarines or unmanned underwater vehicles from transmitting wireless VLF signals from underwater to shore or air. Overcoming the boundary between water and air

**Table 2 | State-of-the-art performance of magnetoelectric components, goals and potential approaches for IoT applications**

ME IoT applications	Current state-of-the-art	Goal	Possible approach
ME-based memory and logic	Proposed MESO-coupled logic device	Multiferroic component voltage requirement of ~100 mV	Reduce the coercive field of the multiferroic component either through pushing the BiFeO <sub>3</sub> to a phase boundary or selecting another multiferroic material
ME magnetometers	Detection of ~3 fT/√Hz at 24 kHz	Detection of fT magnetic fields at 0.01 Hz–1 kHz	Novel ME sensor designs, new schemes for noise cancellation
UHF ME antennas	Antenna gain of ~18 dBi, ground plane immunity, antenna arrays, WPT and magnetic field sensing	Improved antenna efficiency, integration of new materials and so on	Integration of low-loss magnetic materials such as yttrium iron garnet into ME antennas, micromagnetic and acoustic simulation for design optimization
VLF ME antennas	Transmission distance of over 120 m in air, high data rates of 2 kbps	Far-field demonstration through lossy media, that is, seawater or underground	ME antenna arrays, nonlinear coupling, vacuum packaging and so on
WPT	>10× improved WPT efficiency over resonant coil-to-coil WPT at long distances	Demonstration in real IoT applications at large distances	New ME antennas for WPT, implementation of WPT using ME antennas for IoT, and so on
Nonreciprocity via magnetoacoustic effects	Demonstration of nonreciprocity in amplitude and phase	Demonstration of functioning isolators and circulators with low insertion loss	New magnetoacoustic isolator and circulator designs and new materials for low insertion loss
ME quantum transduction	ADFMR control of nitrogen-vacancy centres with high efficiency	Coherent control of nitrogen-vacancy centres using acoustically driven spin waves with low noise	Heterogeneous integration of low-loss magnetic materials, driving nitrogen-vacancy centres in diamond with ADFMR devices exhibiting strong absorption at the frequency and magnetic field matching the spin resonance of a nitrogen-vacancy centre

ADFMR, acoustic driven ferromagnetic resonance; IoT, internet of things; ME, magnetoelectric; MESO, magnetoelectric spin-orbit device; UHF, ultra-high-frequency operation; VLF, very-low-frequency operation; WPT, wireless power transfer.

for wireless communications has been a persistent challenge<sup>199</sup>. The ultra-compact mobile VLF ME antenna arrays offer a promising path to future bi-directional water-air or water-shore and underground wireless communications<sup>29,30</sup>.

Besides wireless communication, ME antennas have excellent performance for wireless power transfer. ME antennas have demonstrated efficiency one order of magnitude higher than resonant coil-to-coil links for wireless power transfer at large distances with significantly improved tolerance of misalignment over inductive coupling and resonant inductive coupling. With the combined advantages, ME wireless power transfer would be an excellent way of powering mobile robots, unmanned underwater vehicles, etc. Moreover, ultra-compact mobile magnetoelectric antennas and microsystems can be used for highly efficient simultaneous wireless information and power transfer, which is critical for IoT systems and allows the transfer of both information and power simultaneously to the end devices.

## Outlook

ME devices demonstrate excellent performance in wireless communication, magnetic sensing and energy transduction with good energy efficiency. ME N/MEMS, such as smart ME antennas, exhibit multifunctionality and versatility in diverse IoT scenarios, combining data communication, magnetic field sensing and wireless energy transfer (Table 2). Fully leveraging the potential of ME materials and devices for IoT remains a work in progress.

Integrating ME materials with CMOS-compatible processes is a significant challenge for use in IoT. For instance, low-loss magnetic materials, such as yttrium iron garnet, require high processing temperatures exceeding 700 °C, breaching the thermal limits of back-end-of-line CMOS processing. Low-loss magnetostrictive films, such as FeGaB and FeGaC, are promising alternatives with their low deposition temperature and CMOS compatibility.

ME magnetometers exhibit a magnetic sensing capability of fT Hz<sup>-0.5</sup> at 24 kHz (C.D. et al., manuscript in preparation). The goal, however, is to extend this sensitivity to a broader frequency range, spanning from 0.01 Hz to 1 kHz, while maintaining detection thresholds on the order of fT. Novel ME sensor designs and new schemes for noise cancellation need to be explored.

Boosting the gain and the radiation efficiency of UHF ME antennas is essential for IoT applications such as WPT, magnetic sensing and communication. Despite experimental demonstration of high-gain UHF ME antennas, the design and simulation of ME antennas for improving their performance is an open challenge. An efficient bulk acoustic wave-mediated multiferroic antenna was designed and simulated using the finite-difference time-domain technique<sup>200</sup>. However, being that the simulation model was limited to 1D, its abilities to fully capture the spin wave–acoustic wave interactions and, therefore, the ability to design high-performance ME antennas are limited. Two-dimensional and three-dimensional micromagnetic and acoustic simulation platforms need to be developed that capture the complex interactions of spin waves and acoustic waves to optimize the design of UHF ME antenna units and array structures. Additionally, the magnetic damping of the magnetostrictive layer, typically on the order of 10<sup>-4</sup> to 10<sup>-3</sup>, is another concern that degrades the gain and radiation efficiency of ME antennas. Future efforts need to incorporate low magnetic loss (magnetic damping on the order of 10<sup>-5</sup>) materials, such as yttrium iron garnet, into the ME NEMS antennas, to boost antenna gain and radiation efficiency.

VLF ME antennas ensure robust performance in lossy mediums such as water and ground owing to reduced EM signal attenuation for magnetic field components, and their compact size allows low-frequency operations that reduce energy loss and dissipation. Additionally, VLF magnetoelectric antennas can significantly enhance data transmission rates by over ten times via nonlinear modulation techniques.

As of the beginning of 2024, ME VLF antennas have only demonstrated near-field communication. An open challenge for VLF ME antennas is to demonstrate VLF ME transmitters with radiation in the far field, and subsequent packaging and testing in a seawater environment. Besides, nonlinear coupling among ME antennas in a compact array is also interesting to explore for the potential realization of frequency synchronization and gain enhancement with optimal interspacing and bias conditions. The nonlinear coupling can enable multiple responsive antennas optimally driven by a single active element, which offers promising avenues for potential minimization of ME antenna array system dimensions. Moreover, novel nonlinear antenna modulation techniques with higher-order harmonic sideband signal output would be another interesting direction to further break the limit of data rates and bandwidth of ME antennas. The emerging approaches combining nonlinear antenna modulation and nonlinear coupling among ME antennas hold significant promise for ushering in a new generation of compact, economically efficient ME antenna arrays with wide bandwidth operation and high data rates.

Existing ME antenna technologies have exhibited over tenfold improvements in WPT efficiency over traditional resonant coil-to-coil methods at long distances, but the challenge lies in demonstrating these capabilities in real-world IoT applications over large distances. New ME antennas for WPT need to be designed and optimized, and demonstration of the full strength of ME antennas for IoT has yet to be carried out on WPT, data communication, magnetic and vibration sensing, and so on.

In the sub-field of nonreciprocal magnetoacoustic RF components, the accumulation of nonreciprocal phase surpasses  $\pi$  radians under various field conditions, offering potential for effective circulator development<sup>28</sup>. The objective is to create highly efficient magnetoacoustic isolators and circulators with low insertion loss, which requires optimal design via theory and simulation, and follow up with experimental verification.

In terms of ME quantum transduction, with efficient control of nitrogen-vacancy centres by ADFMR, future work is oriented towards coherent control of nitrogen-vacancy centres using well-defined spin waves, with an emphasis on low noise metrics. Heterogeneous integration of low-loss magnetic materials in ADFMR devices for manipulation of nitrogen-vacancy centres in a diamond crystal is desired for maintaining spin wave magnitude and propagation distance and enhancing the relaxation time  $T_1$  and coherence time  $T_2$ . The long  $T_1$  and  $T_2$  ensure that quantum information transferred from acoustic phonons and then stored in magnons can maintain a sufficient lifetime without notable decay or loss owing to relaxation or decoherence, whereas the strong magnitude and long propagation length of spin wave make it possible to realize the long-distance communication of quantum information between various quantum information storage and processing platforms via magnons.

Published online: 7 May 2024

## References

- Imran, M. A., Zoha, A., Zhang, L. & Abassi, Q. H. Grand challenges in IoT and sensor networks. *Front. Comms. Net.* <https://doi.org/10.3389/frcmn.2020.619452> (2020).
- Suchtelen, J. V. Product properties: a new application of composite materials. *Philips Res. Rep.* **27**, 28–37 (1972).
- Van Run, A. M. J. G., Terrell, D. R. & Scholing, J. H. An in situ grown eutectic magnetoelastic composite material. *J. Mater. Sci.* **9**, 1710–1714 (1974).
- Ryu, J., Carazo, A. V., Uchino, K. & Kim, H.-E. Magnetoelastic properties in piezoelectric and magnetostrictive laminate composites. *Jpn. J. Appl. Phys.* **40**, 4948 (2001).
- Srinivasan, G. et al. Magnetoelastic bilayer and multilayer structures of magnetostrictive and piezoelectric oxides. *Phys. Rev. B* **64**, 214408 (2001).

- Dong, S. X., Li, J. F. & Viehland, D. Longitudinal and transverse magnetoelastic voltage coefficients of magnetostrictive/piezoelectric laminate composite: theory. *IEEE Trans. Ultrason. Ferroelectr. Freq. Control* **50**, 1253–1261 (2003).
- Dong, S. X., Li, J. F. & Viehland, D. Giant magneto-electric effect in laminate composites. *IEEE Trans. Ultrason. Ferroelectr. Freq. Control.* **50**, 1236–1239 (2003).
- Bichurin, M. I. et al. Resonance magnetoelastic effects in layered magnetostrictive-piezoelectric composites. *Phys. Rev. B* **68**, 132408 (2003).
- Wang, J. et al. Epitaxial BiFeO<sub>3</sub> multiferroic thin film heterostructures. *Science* **299**, 1719–1722 (2003).
- Zheng, H. et al. Multiferroic BaTiO<sub>3</sub>-CoFe<sub>2</sub>O<sub>4</sub> nanostructures. *Science* **303**, 661–663 (2004).
- Srinivasan, G. & Fetisov, Y. K. Microwave magnetoelastic effects and signal processing devices. *Integr. Ferroelectr.* **83**, 89–98 (2006).
- Zhai, J. Y., Xing, Z. P., Dong, S. X., Li, J. F. & Viehland, D. Detection of pico-Tesla magnetic fields using magneto-electric sensors at room temperature. *Appl. Phys. Lett.* <https://doi.org/10.1063/1.2172706> (2006).
- Dong, S. X., Zhai, J. Y., Li, J. F. & Viehland, D. Near-ideal magnetoelasticity in high-permeability magnetostrictive/piezofiber laminates with a (2-1) connectivity. *Appl. Phys. Lett.* <https://doi.org/10.1063/1.2420772> (2006).
- Lou, J. et al. Soft magnetism, magnetostriction, and microwave properties of FeGaB thin films. *Appl. Phys. Lett.* **91**, 182504 (2007).
- This article reports the deposition of FeGaB films with excellent magnetic softness, high saturation magnetization, high self-biased FMR frequency, narrow FMR linewidth and a high-saturation magnetostriction constant, showing great potential for tunable magnetoelastic microwave devices and other RF or microwave magnetic device applications.**
- Maruyama, T. et al. Large voltage-induced magnetic anisotropy change in a few atomic layers of iron. *Nat. Nanotech.* **4**, 158–161 (2009).
- Liu, M. et al. Giant electric field tuning of magnetic properties in multiferroic ferrite/ferroelectric heterostructures. *Adv. Funct. Mater.* **19**, 1826–1831 (2009).
- Lou, J., Liu, M., Reed, D., Ren, Y. H. & Sun, N. X. Giant electric field tuning of magnetism in novel multiferroic FeGaB/lead zinc niobate-lead titanate (PZN-PT) heterostructures. *Adv. Mater.* **21**, 4711–4715 (2009).
- This article reports a novel multiferroic FeGaB/PZN-PT heterostructure with giant electrical field tunability of the ferromagnetic resonance frequency, which is promising for wide-band electrostatically tunable microwave resonators.**
- Lage, E. et al. Exchange biasing of magnetoelastic composites. *Nat. Mater.* **11**, 523–529 (2012).
- Nan, T. X., Hui, Y., Rinaldi, M. & Sun, N. X. Self-biased 215 MHz magnetoelastic NEMS resonator for ultra-sensitive DC magnetic field detection. *Sci. Rep.* **3**, 1985 (2013).
- This article demonstrates a novel compact, power-efficient, CMOS-compatible NEMS magnetic sensor based on an AlN/(FeGaB/Al<sub>2</sub>O<sub>3</sub>)<sub>10</sub> bulk acoustic resonator, showing ultra-high magnetic field sensitivity for low-frequency AC magnetic field and a low limit of detection of DC magnetic fields.**
- Heron, J. T. et al. Deterministic switching of ferromagnetism at room temperature using an electric field. *Nature* **516**, 370–373 (2014).
- Sun, N. X. & Lim, M. Magnetoelastic very low frequency communication system. US patent 10,720,564 (2016).
- Nan, T. et al. Acoustically actuated ultra-compact NEMS magnetoelastic antennas. *Nat. Commun.* **8**, 296 (2017).
- This article reports acoustically actuated nanomechanical magnetoelastic antennas with thin-film FBAR ferromagnetic-piezoelectric thin-film heterostructures, which demonstrates one to two orders of magnitude miniaturization over state-of-the-art compact antennas without performance degradation and have potential implications for portable wireless communication systems.**
- Kittmann, A. et al. Wide band low noise love wave magnetic field sensor system. *Sci. Rep.* **8**, 278 (2018).
- This article presents a wide-band low-noise Love wave magnetic field sensor system that utilizes magnetoelastically induced changes of the shear modulus, showing an extremely low magnetic noise level, wide bandwidth and dynamic range.**
- Manipatruni, S. et al. Scalable energy-efficient magnetoelastic spin-orbit logic. *Nature* **565**, 35–42 (2019).
- This article proposes a scalable spintronic logic device that operates via spin-orbit transduction combined with magnetoelastic switching and enables the development of multi-generational computing, showing superior switching energy, lower switching voltage and enhanced logic density in comparison with CMOS technology and ultra-low standby power critical to modern computing.**
- Shah, P. J. et al. Giant nonreciprocity of surface acoustic waves enabled by the magnetoelastic interaction. *Sci. Adv.* **6**, eabc5648 (2020).
- This article reports giant nonreciprocity in the transmission of SAWs on lithium niobate substrate coated with ferromagnet-insulator-ferromagnet (FeGaB/Al<sub>2</sub>O<sub>3</sub>/FeGaB) multilayer structure, which shows great potential for power-efficient RF or microwave isolators.**
- Zaebimbashi, M. et al. Ultra-compact dual-band smart NEMS magnetoelastic antennas for simultaneous wireless energy harvesting and magnetic field sensing. *Nat. Commun.* **12**, 3141 (2021).
- This article shows an ultra-compact dual-band smart nanoelectromechanical systems ME antenna that can perform overwhelmingly efficient wireless energy harvesting and ultra-small neural magnetic field sensing.**

27. Liang, X. F. et al. Experimental demonstration of ground plane immunity for magnetolectric antennas. In *2022 IEEE MTT-S International Microwave Workshop Series on Advanced Materials and Processes for RF and THz Applications (IMWS-AMP)* (IEEE, 2022).
28. Bas, D. A. et al. Nonreciprocity of phase accumulation and propagation losses of surface acoustic waves in hybrid magnetoelastic heterostructures. *Phys. Rev. Appl.* **18**, 044003 (2022).  
**This article reports the observation of nonreciprocal phase accumulation easily exceeding  $\pi$  radians over a broad range of field conditions in a magnetoelastic heterostructure (FeGaB/Al<sub>2</sub>O<sub>3</sub>/FeGaB) on a LiNbO<sub>3</sub> single crystal owing to hybridized SAWs and spin waves, paving a pathway for the development of an effective circulator.**
29. Dong, C., He, Y., Liu, X. & Sun, N. X. VLF mechanical antenna arrays for underwater wireless communications. In *Proc. of the 16th International Conference on Underwater Networks & Systems* (ACM, 2022).  
**This article reports a 12-unit high-quality-factor (Q) PZT-Metglas ME antenna array with significant enhancement of one order of magnitude radiation field and efficiency over a single antenna unit, showing the great potential of a large ME antenna array for underwater wireless communications.**
30. Dong, C. Z. et al. A portable very low frequency (VLF) communication system based on acoustically actuated magnetolectric antennas. *IEEE Antennas Wirel. Propag. Lett.* **19**, 398–402 (2020).  
**This article demonstrates very low frequency (VLF) magnetolectric antennas and communication systems based on strain-mediated magnetolectric resonators operating at their electromechanical resonance, achieving a long-distance, low-power-consumption and enhanced transmission data rate via direct antenna modulation.**
31. Liang, X. J. et al. Mechanically driven solidly mounted resonator-based nanoelectromechanical systems magnetolectric antennas. *Adv. Eng. Mater.* <https://doi.org/10.21203/rs.3.rs-1118802/v1> (2023).  
**This article demonstrates 1.75 GHz SMR NEMS ME antennas on a Bragg acoustic resonant reflector, showing a high antenna gain, robust mechanical properties, high power handling capability, CMOS-compatible fabrication process and dramatic miniaturization promising for future antenna systems.**
32. Will-Cole, A. R. et al. Tutorial: piezoelectric and magnetolectric N/MEMS — materials, devices and applications. *J. Appl. Phys.* **131**, 241101 (2022).
33. Heron, J. T., Schlom, D. G. & Ramesh, R. Electric field control of magnetism using BiFeO<sub>3</sub>-based heterostructures. *Appl. Phys. Rev.* <https://doi.org/10.1063/1.4870957> (2014).
34. Manipatruni, S., Nikonov, D. E. & Young, I. A. Beyond CMOS computing with spin and polarization. *Nat. Phys.* **14**, 338–343 (2018).
35. Lou, J., Reed, D., Liu, M. & Sun, N. Electrostatically tunable magnetolectric inductors with large inductance tunability. *Appl. Phys. Lett.* **94**, 112508 (2009).
36. Lou, J. *Electrostatically Tunable Microwave Multiferric Heterostructures with Novel Magnetic Materials*. PhD thesis, Northeastern Univ. (2010).
37. Bas, D. A. et al. Acoustically driven ferromagnetic resonance in diverse ferromagnetic thin films. *IEEE Trans. Magn.* <https://doi.org/10.1109/TMAG.2020.3019214> (2021).
38. Awschalom, D. D. et al. Quantum engineering with hybrid magnonic systems and materials (invited paper). *IEEE Trans. Quantum Eng.* **2**, 1–36 (2021).
39. Labanowski, D. et al. Voltage-driven, local, and efficient excitation of nitrogen-vacancy centers in diamond. *Sci. Adv.* **4**, eaat6574 (2018).  
**This article reports voltage-driven, local and efficient excitation of nitrogen-vacancy centres via SAW-driven ferromagnetic resonance and nitrogen vacancy-magnon coupling, showing a new pathway that combines acoustics and magnonics for highly energy-efficient and local excitation of nitrogen-vacancy centres for integrated, on-chip, atomic magnetic sensors.**
40. Solanki, A. B. et al. Electric field control of interaction between magnons and quantum spin defects. *Phys. Rev. Res.* **4**, L012025 (2022).  
**This article reports electric field control of magnon–nitrogen vacancy centre via CoFeB/PMN-PT multiferric composite and proposes magnon-based hybrid electric field sensors to improve the DC electric field sensitivity of single-spin sensors.**
41. Dong, C. Z. et al. Acoustically actuated magnetolectric antenna arrays for VLF radiation enhancement. In *2022 IEEE International Symposium on Phased Array Systems & Technology (Past)* (IEEE, 2022).
42. Vaz, C. A. Electric field control of magnetism in multiferric heterostructures. *J. Phys. Condens. Matter* **24**, 333201 (2012).
43. Spaldin, N. A. & Ramesh, R. Advances in magnetolectric multiferrics. *Nat. Mater.* **18**, 203–212 (2019).
44. Yang, J. J. et al. Electric field manipulation of magnetization at room temperature in multiferric CoFe<sub>2</sub>O<sub>4</sub>/Pb(Mg<sub>1/3</sub>Nb<sub>2/3</sub>)<sub>0.7</sub>Ti<sub>0.3</sub>O<sub>3</sub> heterostructures. *Appl. Phys. Lett.* <https://doi.org/10.1063/1.3143622> (2009).
45. Liu, M. et al. Electrical tuning of magnetism in Fe<sub>3</sub>O<sub>4</sub>/PZN-PT multiferric heterostructures derived by reactive magnetron sputtering. *J. Appl. Phys.* <https://doi.org/10.1063/1.3354104> (2010).
46. Nan, T. X. et al. Quantification of strain and charge co-mediated magnetolectric coupling on ultra-thin permalloy/PMN-PT interface. *Sci. Rep.* **4**, 3688 (2014).
47. Zhou, W. P. et al. Electric field manipulation of magnetic and transport properties in SrRuO<sub>3</sub>/Pb(Mg<sub>1/3</sub>Nb<sub>2/3</sub>)O<sub>3</sub>-PbTiO<sub>3</sub> heterostructure. *Sci. Rep.* **4**, 6991 (2014).
48. Li, M. H. et al. Ultra-sensitive NEMS magnetolectric sensor for picotesla DC magnetic field detection. *Appl. Phys. Lett.* **110**, 143510 (2017).
49. Liang, X. F. et al. Mechanically driven SMR-based MEMS magnetolectric antennas. In *2020 IEEE International Symposium on Antennas and Propagation and North American Radio Science Meeting* 661–662 (IEEE, 2020).
50. Su, J. X. et al. AlScN-based MEMS magnetolectric sensor. *Appl. Phys. Lett.* **117** (2020).
51. Piazza, G., Felmetser, V., Muralt, P., Olsson, R. H. & Ruby, R. Piezoelectric aluminum nitride thin films for microelectromechanical systems. *MRS Bull.* **37**, 1051–1061 (2012).
52. Tasnadi, F. et al. Origin of the anomalous piezoelectric response in wurtzite ScAl<sub>3-x</sub>N Alloys. *Phys. Rev. Lett.* **104**, 137601 (2010).
53. Rabiei, P. & Steier, W. H. Lithium niobate ridge waveguides and modulators fabricated using smart guide. *Appl. Phys. Lett.* **86**, 161115 (2005).
54. Churaev, M. et al. A heterogeneously integrated lithium niobate-on-silicon nitride photonic platform. *Nat. Commun.* **14**, 3499 (2023).
55. Dong, C. Z. et al. Characterization of magnetomechanical properties in FeGaB thin films. *Appl. Phys. Lett.* **113**, 262401 (2018).
56. Liang, X. et al. Soft magnetism, magnetostriction, and microwave properties of Fe-Ga-C alloy films. *IEEE Magn. Lett.* <https://doi.org/10.1109/LMAG.2018.2889630> (2019).
57. Will-Cole, A. R. et al. Application of Bayesian optimization and regression analysis to ferromagnetic materials development. *IEEE Trans. Magn.* <https://doi.org/10.1109/TMAG.2021.3125250> (2022).
58. Meisenheimer, P. B. et al. Engineering new limits to magnetostriction through metastability in iron-gallium alloys. *Nat. Commun.* **12**, 2757 (2021).
59. Acosta, A. et al. Underlayer effect on the soft magnetic, high frequency, and magnetostrictive properties of FeGa thin films. *J. Appl. Phys.* **128**, 013903 (2020).
60. Gilbert, T. L. A phenomenological theory of damping in ferromagnetic materials. *IEEE Trans. Magn.* **40**, 3443–3449 (2004).
61. Spencer, E. G., Lecraw, R. C. & Clogston, A. M. Low-temperature line-width maximum in yttrium iron garnet. *Phys. Rev. Lett.* **3**, 32 (1959).
62. Ding, J., Liu, T., Chang, H. C. & Wu, M. Z. Sputtering growth of low-damping yttrium-iron-garnet thin films. *IEEE Magn. Lett.* <https://doi.org/10.1109/LMAG.2020.2989687> (2020).
63. Yu, H. M. et al. Magnetic thin-film insulator with ultra-low spin wave damping for coherent nanomagnonics. *Sci. Rep.* **4**, 6848 (2014).
64. Maendl, S., Stasinopoulos, I. & Grundler, D. Spin waves with large decay length and few 100 nm wavelengths in thin yttrium iron garnet grown at the wafer scale. *Appl. Phys. Lett.* **111**, 012403 (2017).
65. Makino, H., Nakamura, S. & Matsumi, K. Lattice parameter variations in Czochralski grown gadolinium gallium garnet single crystals. *Jpn. J. Appl. Phys.* **15**, 415–419 (1976).
66. Liu, M. C. et al. Atomic-scale structure and chemistry of YIG/GGG. *AIP Adv.* **8**, 085117 (2018).
67. Jermain, C. L. et al. Increased low-temperature damping in yttrium iron garnet thin films. *Phys. Rev. B* **95**, 174411 (2017).
68. Shigematsu, E. et al. Significant reduction in spin pumping efficiency in a platinum/yttrium iron garnet bilayer at low temperature. *Appl. Phys. Express* **9**, 053002 (2016).
69. Will-Cole, A. R. et al. Negligible magnetic losses at low temperatures in liquid phase epitaxy grown Y<sub>3</sub>Fe<sub>5</sub>O<sub>12</sub> films. *Phys. Rev. Mater.* **7**, 054411 (2023).
70. Guo, S., McCullian, B., Chris Hammel, P. & Yang, F. Low damping at few-K temperatures in Y<sub>3</sub>Fe<sub>5</sub>O<sub>12</sub> epitaxial films isolated from Gd<sub>2</sub>O<sub>3</sub> substrate using a diamagnetic Y<sub>3</sub>Sc<sub>2.5</sub>Al<sub>2.5</sub>O<sub>12</sub> spacer. *J. Magn. Magn. Mater.* **562**, 169795 (2022).
71. Izuwara, T. et al. Single-crystal barium titanate thin films by ion sputtering. *Appl. Phys. Lett.* **82**, 616–618 (2003).
72. Levy, M., Osgood, R. M., Kumar, A. & Bakhru, H. Crystal ion sputtering of single-crystal magnetic garnet films. *J. Appl. Phys.* **83**, 6759–6761 (1998).  
**This article reports the epitaxial liftoff of high-quality and low-loss single-crystal YIG and bismuth-substituted YIG thin films, crucial to the fabrication of YIG-based ME antenna with low damping and strong magnon-phonon coupling.**
73. Prasad, B. et al. Ultralow voltage manipulation of ferromagnetism. *Adv. Mater.* <https://doi.org/10.1002/adma.202001943> (2020).  
**This article demonstrates the ultra-low-voltage magneto-electric switching of a magnetoresistive element in multiferric BiFeO<sub>3</sub>, providing great opportunities for the realization of attojoule-class nonvolatile memories.**
74. Xiaoxi, H. et al. Manipulating chiral-spin transport with ferroelectric polarization. Preprint at <https://doi.org/10.48550/arXiv.2306.02185> (2023).
75. Nakayama, H. et al. Rashba-Edelstein magnetoresistance in metallic heterostructures. *Phys. Rev. Lett.* **117**, 116602 (2016).
76. Hoffmann, A. & Bader, S. D. Opportunities at the frontiers of spintronics. *Phys. Rev. Appl.* **4**, 047001 (2015).
77. Li, J. et al. Ultrafast polarization switching in thin-film ferroelectrics. *Appl. Phys. Lett.* **84**, 1174–1176 (2004).
78. Parsonnet, E. et al. Toward intrinsic ferroelectric switching in multiferric BiFeO<sub>3</sub>. *Phys. Rev. Lett.* **125**, 067601 (2020).
79. Rabe, K. M., Ahn, C. H. & Triscone, J.-M. (eds) *Physics of Ferroelectrics: A Modern Perspective* (Springer, 2007).
80. Gajek, M. et al. Tunnel junctions with multiferric barriers. *Nat. Mater.* **6**, 296–302 (2007).
81. Garcia, V. et al. Ferroelectric control of spin polarization. *Science* **327**, 1106–1110 (2010).
82. Pantel, D., Goetze, S., Hesse, D. & Alexe, M. Reversible electrical switching of spin polarization in multiferric tunnel junctions. *Nat. Mater.* **11**, 289–293 (2012).
83. Li, P. et al. Electric field manipulation of magnetization rotation and tunneling magnetoresistance of magnetic tunnel junctions at room temperature. *Adv. Mater.* **26**, 4320–4325 (2014).
84. Zhao, Z. et al. Giant voltage manipulation of MgO-based magnetic tunnel junctions via localized anisotropic strain: a potential pathway to ultra-energy-efficient memory technology. *Appl. Phys. Lett.* **109**, 092403 (2016).



85. Chen, A. et al. Giant nonvolatile manipulation of magnetoresistance in magnetic tunnel junctions by electric fields via magnetoelectric coupling. *Nat. Commun.* **10**, 243 (2019). **This article reports the efficient modulation of the magnetic tunnel junction through strain-mediated magnetoelectric coupling and realizes a giant, reversible and nonvolatile electric-field manipulation of magnetoresistance, offering significant fundamental insight into information storage towards low-power spintronic devices.**
86. Wang, Y., Li, J. & Viehland, D. Magnetoelctrics for magnetic sensor applications: status, challenges and perspectives. *Mater. Today* **17**, 269–275 (2014).
87. Elzenheimer, E., Laufs, H., Sander-Thömmes, T. & Schmidt, G. Magnetoencephalography of an electrically stimulated arm nerve. *CDBME*, **4**, 363–366 (2018).
88. Cohen, D. & Givler, E. Magnetomyography: magnetic fields around the human body produced by skeletal muscles. *Appl. Phys. Lett.* **21**, 114–116 (2003).
89. Zuo, S., Heidari, H., Farina, D. & Nazarpour, K. Miniaturized magnetic sensors for implantable magnetomyography. *Adv. Mater. Technol.* **5**, 2000185 (2020).
90. Uchikawa, Y. & Kotani, M. Measurement of magnetic field produced from the human body. *IEEE Trans. J. Magn. Jpn.* **7**, 600–607 (1992).
91. Granata, C., Vettoliere, A. & Russo, M. An ultralow noise current amplifier based on superconducting quantum interference device for high sensitivity applications. *Rev. Sci. Instrum.* **82**, 013901 (2011).
92. Shen, Y. et al. Effective optimization of magnetic noise for a Metglas/Pb(Zr,Ti)O<sub>3</sub> magnetoelectric sensor array in an open environment. *Mater. Lett.* **91**, 307–310 (2013).
93. Yarar, E. et al. Inverse bilayer magnetoelectric thin film sensor. *Appl. Phys. Lett.* **109**, 022901 (2016).
94. Hayes, P. et al. Electrically modulated magnetoelectric sensors. *Appl. Phys. Lett.* **108**, 182902 (2016).
95. Salzer, S. et al. Noise limits in thin-film magnetoelectric sensors with magnetic frequency conversion. *IEEE Sens. J.* **18**, 596–604 (2018).
96. Kirchhof, C. et al. Giant magnetoelectric effect in vacuum. *Appl. Phys. Lett.* <https://doi.org/10.1063/1.4810750> (2013).
97. Viehland, D., Wuttig, M., Mccord, J. & Quandt, E. Magnetoelectric magnetic field sensors. *MRS Bull.* **43**, 834–840 (2018).
98. Jahns, R., Greve, H., Woltermann, E., Quandt, E. & Knochel, R. Sensitivity enhancement of magnetoelectric sensors through frequency-conversion. *Sens. Actuators A Phys.* **183**, 16–21 (2012).
99. Dong, S. X., Cheng, J. R., Li, J. F. & Viehland, D. Enhanced magnetoelectric effects in laminate composites of Terfenol-D/Pb(Zr,Ti)O<sub>3</sub> under resonant drive. *Appl. Phys. Lett.* **83**, 4812–4814 (2003).
100. Petrie, J. et al. Shifting the operating frequency of magnetoelectric sensors. *J. Appl. Phys.* <https://doi.org/10.1063/1.3677840> (2012).
101. Spetzler, B. et al. Magnetoelastic coupling and delta-E effect in magnetoelectric torsion mode resonators. *Sensors* **21**, 2022 (2021).
102. Schell, V. et al. Exchange biased surface acoustic wave magnetic field sensors. *Sci. Rep.* **13**, 8446 (2023).
103. Chen, J. C. et al. A wireless millimeter magnetoelectric implant for the endovascular stimulation of peripheral nerves. *Nat. Biomed. Eng.* **6**, 706–716 (2022).
104. Liang, X. F., Chen, H. H., Sun, N., Lin, H. & Sun, N. X. Novel acoustically actuated magnetoelectric antennas. In *2018 IEEE Antennas and Propagation Society International Symposium on Antennas and Propagation & USNC/URSI National Radio Science Meeting 2189–2190* (IEEE, 2018).
105. Hansen, P. & Rodriguez, D. High power VLF/LF transmitting antennas — Wheeler’s circuit approximations applied to power limitations. In *2012 IEEE Antennas and Propagation Society International Symposium (APSURSI)* (IEEE, 2012).
106. He, Y. *Magnetic and Magnetoelectric Devices for Communication and Energy Harvesting Applications*. PhD thesis, Northeastern Univ. (2023).
107. Kemp, M. A. et al. A high Q piezoelectric resonator as a portable VLF transmitter. *Nat. Commun.* **10**, 1715 (2019).
108. Guo, Y., Yang, C. & Huang, B. Design of flexible FeCoSiB/ZnO thin-film multiferroic module for low-frequency energy harvesting. *Energies* **16**, 5049 (2023).
109. He, W. & Liu, S. H. A magnetoelectric energy harvester for low-frequency vibrations and human walking. *J. Magn. Magn. Mater.* **542**, 168609 (2022).
110. Yekta, H. B. & Fakhari, V. A novel optimized design of an energy harvester using magnetoelectric transducers. *J. Intell. Mater. Syst. Struct.* <https://doi.org/10.1177/1045389x231167070> (2023).
111. Leung, C. M. et al. Highly efficient solid state magnetoelectric gyrators. *Appl. Phys. Lett.* **111**, 122904 (2017).
112. Niu, Y. P. & Ren, H. A high efficiency standalone magnetoelectric energy converter based on Terfenol-D and PZT laminate. *Appl. Phys. Lett.* **118**, 044101 (2021).
113. Yu, Z. et al. MagNI: a magnetoelectrically powered and controlled wireless neurostimulating implant. *IEEE Trans. Biomed. Circuits Syst.* **14**, 1241–1252 (2020).
114. Lin, J. C. Radio-frequency radiation safety and health. *URSI Radio. Sci. Bull.* **2011**, 95–100 (2011).
115. Ghosh, R. et al. Energy-harvesting performance in a LaFe<sub>2</sub>O<sub>6</sub>/P(VDF-HFP) nanocomposite by boosting the magnetoelectric effect. *ACS Appl. Nano Mater.* **8**, 6841–6848 (2023).
116. Pabba, D. P. et al. Flexible magnetoelectric PVDF–CoFe<sub>2</sub>O<sub>4</sub> fiber films for self-powered energy harvesters. *Ceram. Int.* **49**, 31096–31105 (2023).
117. Zaeimbashi, M. et al. NanoNeuroRFID: a wireless implantable device based on magnetoelectric antennas. *IEEE J. Electromagn. RF Microw. Med. Biol.* **3**, 206–215 (2019).
118. Yu, Z. G. et al. A wireless network of 8.8-mm<sup>3</sup> bio-implants featuring adaptive magnetoelectric power and multi-access bidirectional telemetry. In *2022 IEEE Radio Frequency Integrated Circuits Symposium (RFIC)* 47–50 (IEEE, 2022).
119. Yu, Z. H. et al. Magnetoelectric backscatter communication for millimeter-sized wireless biomedical implants. *GetMobile Mob. Comput. Commun. Rev.* **27**, 23–27 (2023).
120. He, Y., Luo, B. & Sun, N.-X. Integrated magnetics and magnetoelectrics for sensing, power, RF, and microwave electronics. *IEEE J. Microw.* **1**, 908–929 (2021).
121. Cheng, Y. X., Peng, B., Hu, Z. Q., Zhou, Z. Y. & Liu, M. Recent development and status of magnetoelectric materials and devices. *Phys. Lett. A* **382**, 3018–3025 (2018).
122. Tatarenko, A. S., Murthy, D. V. B. & Srinivasan, G. Hexagonal ferrite-piezoelectric composites for dual magnetic and electric field tunable 8-25 GHz microstripline resonators and phase shifters. *Microw. Opt. Technol. Lett.* **54**, 1215–1218 (2012).
123. Tatarenko, A. S., Srinivasana, G. & Bichurin, M. I. Magnetoelectric microwave phase shifter. *Appl. Phys. Lett.* <https://doi.org/10.1063/1.2198111> (2006).
124. Yang, X. et al. Compact and low loss phase shifter with low bias field using partially magnetized ferrite. *IEEE Trans. Magn.* **49**, 3882–3885 (2013).
125. Yang, X. et al. Voltage tunable multiferroic phase shifter with YIG/PMN-PT heterostructure. *IEEE Microw. Wirel. Compon. Lett.* **24**, 191–193 (2014).
126. Ustinov, A., Srinivasan, G. & Kalinikos, B. Ferrite-ferroelectric hybrid wave phase shifters. *Appl. Phys. Lett.* **90**, 031913 (2007).
127. Geiler, A. L. et al. Multiferroic heterostructure fringe field tuning of meander line microstrip ferrite phase shifter. *Appl. Phys. Lett.* **96**, 053508 (2010).
128. Tatarenko, A. S. & Srinivasan, G. A strain engineered voltage tunable millimeter-wave ferrite phase shifter. *Microw. Opt. Technol. Lett.* **53**, 261–264 (2011).
129. Yun, E. J., Jung, M., Cheon, C. I. & Nam, H. G. Microfabrication and characteristics of low-power high-performance magnetic thin-film transformers. *IEEE Trans. Magn.* **40**, 65–70 (2004).
130. Wang, X. J. et al. A novel NiZn ferrite integrated magnetic solenoid inductor with a high quality factor at 0.7-6 GHz. *AIP Adv.* **7**, 056606 (2017).
131. Flynn, D., Toon, A., Allen, L., Dhariwal, R. & Desmulliez, M. P. Y. Characterization of core materials for microscale magnetic components operating in the megahertz frequency range. *IEEE Trans. Magn.* **43**, 3171–3180 (2007).
132. Gao, Y. et al. Significantly enhanced inductance and quality factor of GHz integrated magnetic solenoid inductors with FeGaB/Al<sub>2</sub>O<sub>3</sub> multilayer films. *IEEE Trans. Electron. Devices* **61**, 1470–1476 (2014).
133. Gao, Y. et al. Power-efficient voltage tunable RF integrated magnetoelectric inductors with FeGaB/Al<sub>2</sub>O<sub>3</sub> multilayer films. In *2014 IEEE MTT-S International Microwave Symposium (IMS)* (IEEE, 2014).
134. Mullenix, J., El-Ghazaly, A. & Wang, S. X. Integrated transformers with sputtered laminated magnetic core. *IEEE Trans. Magn.* **49**, 4021–4027 (2013).
135. El-Ghazaly, A., White, R. M. & Wang, S. X. Gigahertz-band integrated magnetic inductors. *IEEE Trans. Microw. Theory Tech.* **65**, 4893–4900 (2017).
136. Chen, H. H. et al. Integrated tunable magnetoelectric RF inductors. *IEEE Trans. Microw. Theory Tech.* **68**, 951–963 (2020). **This article demonstrates GHz integrated solenoid magnetoelectric inductors based on FeGaB/Al<sub>2</sub>O<sub>3</sub> multilayer with a high Q factor and giant inductance electrical tunability, greatly improving the integration level and performance of tunable radiofrequency integrated circuits while reducing their power consumption and cost.**
137. Kittel, C. Ferromagnetic resonance. *J. Phys. Radium* **12**, 291–302 (1951).
138. Lin, H. et al. Voltage tunable magnetoelectric inductors with improved operational frequency and quality factor for power electronics. *IEEE Trans. Magn.* <https://doi.org/10.1109/TMAG.2014.2326619> (2015).
139. Zhu, Y., Qiu, G., Chi, K. H., Wang, B. B. T. & Tsai, C. S. A tunable X-band band-pass filter module using YIG/GGG layer on RT/duroid substrate. *IEEE Trans. Magn.* **45**, 4195–4198 (2009).
140. Bi, K., Zhu, W. T., Lei, M. & Zhou, J. Magnetically tunable wideband microwave filter using ferrite-based metamaterials. *Appl. Phys. Lett.* **106**, 173507 (2015).
141. Popov, M. et al. Y-type hexagonal ferrite-based band-pass filter with dual magnetic and electric field tunability. *Sci. Rep.* **13**, 1179 (2023).
142. Popov, M. A., Zavislyak, I. V., Murthy, D. & Srinivasan, G. Dielectric resonance in nickel ferrite for K and Ka-band filters. *Microw. Opt. Technol. Lett.* **56**, 814–818 (2014).
143. Tatarenko, A., Gheevarghese, V. & Srinivasan, G. Magnetoelectric microwave bandpass filter. *Electron. Lett.* **42**, 540–541 (2006).
144. He, Y. F. et al. Integrated tunable bandstop filter using self-biased FeGaB/Al<sub>2</sub>O<sub>3</sub> multilayer thin film. *IEEE Trans. Magn.* <https://doi.org/10.1109/TMAG.2018.2851579> (2018).
145. Pettiford, C., Dasgupta, S., Lou, J., Yoon, S. D. & Sun, N. X. Bias field effects on microwave frequency behavior of PZT/YIG magnetoelectric bilayer. *IEEE Trans. Magn.* **43**, 3343–3345 (2007).
146. Wu, J., Yang, X., Beguhn, S., Lou, J. & Sun, N. X. Nonreciprocal tunable low-loss bandpass filters with ultra-wideband isolation based on magnetostatic surface wave. *IEEE Trans. Microw. Theory Tech.* **60**, 3959–3968 (2012).
147. Lin, H. et al. Integrated non-reciprocal dual H- and E-field tunable bandpass filter with ultra-wideband isolation. In *2015 IEEE MTT-S International Microwave Symposium (IMS)* (IEEE, 2015).
148. Lin, H. et al. Tunable RF band-pass filters based on NEMS magnetoelectric resonators. In *2016 IEEE MTT-S International Microwave Symposium (IMS)* (IEEE, 2016).
149. Semenov, A. et al. Ferrite-ferroelectric layered structures for electrically and magnetically tunable microwave resonators. *Appl. Phys. Lett.* <https://doi.org/10.1063/1.2166489> (2006).
150. Sun, N. X. & Srinivasan, G. Voltage control of magnetism in multiferroic heterostructures and devices. *Spin* **2**, 1240004 (2012).

151. Zhou, J., Reiskarimian, N. & Krishnaswamy, H. 9.8 receiver with integrated magnetic-free N-path-filter-based non-reciprocal circulator and baseband self-interference cancellation for full-duplex wireless. In *2016 IEEE International Solid-State Circuits Conference (ISSCC)* 178–180 (IEEE, 2016).
152. Reiskarimian, N., Dastjerdi, M. B., Zhou, J. & Krishnaswamy, H. 18.2 highly-linear integrated magnetic-free circulator-receiver for full-duplex wireless. In *2017 IEEE International Solid-State Circuits Conference (ISSCC)* (IEEE, 2017).
153. Nagulu, A. & Krishnaswamy, H. Non-magnetic CMOS switched-transmission-line circulators with high power handling and antenna balancing: theory and implementation. *IEEE J. Solid State Circuits* **54**, 1288–1303 (2019).
154. Nagulu, A. et al. Ultra-wideband switched-capacitor delays and circulators-theory and implementation. *IEEE J. Solid State Circuits* **56**, 1412–1424 (2021).
155. Nagulu, A. et al. Nonreciprocal components based on switched transmission lines. In *IEEE Transactions on Microwave Theory and Techniques* 1–20 (IEEE, 2018).
156. Yang, W. G. & Schmidt, H. Acoustic control of magnetism toward energy-efficient applications. *Appl. Phys. Rev.* **8**, 021304 (2021).
157. Heil, J., Luthi, B. & Thalmeier, P. Nonreciprocal surface-acoustic-wave propagation in aluminum. *Phys. Rev. B* **25**, 6515–6517 (1982).
158. Komoriya, G. & Thomas, G. Magnetoelastic-surface waves on YIG substrate. *J. Appl. Phys.* **50**, 6459–6468 (1979).
159. Shimizu, Y., Hasegawas, K. & Yamada, T. Nonreciprocity of SAW velocity on a magnetized ferrite substrate. *Electron. Commun. Jpn.* **63**, 1–7 (1980).
160. Sasaki, R., Nii, Y., Iguchi, Y. & Onose, Y. Nonreciprocal propagation of surface acoustic wave in Ni/LiNbO<sub>3</sub>. *Phys. Rev. B* **95**, 020407 (2017).
161. Xu, M. et al. Nonreciprocal surface acoustic wave propagation via magneto-rotation coupling. *Sci. Adv.* **6**, eabb1724 (2020).
- This article, to our knowledge, firstly reports nonreciprocal acoustic wave attenuation via the magneto-rotation coupling in a perpendicularly anisotropic film, demonstrating a new path for investigating magnon–phonon coupling and an efficient acoustic rectifier tuned by magnetic field.**
162. Ham, W. S. et al. Dzyaloshinskii-Moriya interaction in noncentrosymmetric superlattices. *Npj Comput. Mater.* **7**, 129 (2021).
163. Verba, R., Lisenkov, I., Krivorotov, I., Tiberkevich, V. & Slavin, A. Nonreciprocal surface acoustic waves in multilayers with magnetoelastic and interfacial Dzyaloshinskii-Moriya interactions. *Phys. Rev. Appl.* **9**, 064014 (2018).
164. Grunberg, P. Magnetostatic spin-wave modes of a heterogeneous ferromagnetic double-layer. *J. Appl. Phys.* **52**, 6824–6829 (1981).
165. Verba, R., Bankowski, E. N., Meitzler, T. J., Tiberkevich, V. & Slavin, A. Phase nonreciprocity of microwave-frequency surface acoustic waves in hybrid heterostructures with magnetoelastic coupling. *Adv. Electron. Mater.* **7**, 2100263 (2021).
166. Verba, R., Tiberkevich, V. & Slavin, A. Wide-band nonreciprocity of surface acoustic waves induced by magnetoelastic coupling with a synthetic antiferromagnet. *Phys. Rev. Appl.* **12**, 054601 (2019).
167. Li, Y. et al. Hybrid magnonics: physics, circuits, and applications for coherent information processing. *J. Appl. Phys.* **128**, 130902 (2020).
168. Huang, H. & Tian, Z. T. Topological phonon-magnon hybrid excitations in a two-dimensional honeycomb ferromagnet. *Phys. Rev. B* **104**, 064305 (2021).
169. Clerk, A. A., Lehnert, K. W., Bertet, P., Petta, J. R. & Nakamura, Y. Hybrid quantum systems with circuit quantum electrodynamics. *Nat. Phys.* **16**, 257–267 (2020).
170. Zhang, X., Zou, C.-L., Jiang, L. & Tang, H. X. Cavity magnomechanics. *Sci. Adv.* **2**, e1501286 (2016).
171. Bozhko, D. A., Vasyuchka, V. I., Chumak, A. V. & Serga, A. A. Magnon-phonon interactions in magnon spintronics (Review article). *Low Temp. Phys.* **46**, 383–399 (2020).
172. Bauer, G. E. W., Saitoh, E. & van Wees, B. J. Spin caloritronics. *Nat. Mater.* **11**, 391–399 (2012).
173. Berk, C. et al. Strongly coupled magnon-phonon dynamics in a single nanomagnet. *Nat. Commun.* **10**, 2652 (2019).
174. An, K. et al. Coherent long-range transfer of angular momentum between magnon Kittel modes by phonons. *Phys. Rev. B* **101**, 060407 (2020).
175. Godejohann, F. et al. Magnon polaron formed by selectively coupled coherent magnon and phonon modes of a surface patterned ferromagnet. *Phys. Rev. B* **102**, 144438 (2020).
176. Berk, C. R. & Schmidt, H. A quantum tango between magnons and phonons. *Physics* **13**, 167 (2020).
177. Whiteley, S. J. et al. Spin-phonon interactions in silicon carbide addressed by Gaussian acoustics. *Nat. Phys.* **15**, 490–495 (2019).
178. Bolgar, A. N. et al. Quantum regime of a two-dimensional phonon cavity. *Phys. Rev. Lett.* **120**, 223603 (2018).
179. Satzinger, K. J. et al. Quantum control of surface acoustic-wave phonons. *Nature* **563**, 661–665 (2018).
180. Ji, Y., Zhang, C. & Nan, T. Magnon-phonon-interaction-induced electromagnetic wave radiation in the strong-coupling region. *Phys. Rev. Appl.* **18**, 064050 (2022).
- This article theoretically studies the electromagnetic wave radiation of magnons driven by acoustic phonons in YIG/AlN magnetoelastic antennas with strong magnon–phonon interaction, which demonstrates a substantial enhancement of the antenna radiation efficiency and opens up possibilities of developing ultra-compact magnetoelastic antennas using the hybridized magnon–phonon mode.**
181. Rachford, F. J., Levy, M., Osgood, R. M., Kumar, A. & Bakhru, H. Magnetization and FMR studies of crystal-ion-sliced narrow linewidth gallium-doped yttrium iron garnet. *J. Appl. Phys.* **87**, 6253–6255 (2000).
182. Levy, M., Osgood, R. M., Kumar, A. & Bakhru, H. Epitaxial liftoff of thin oxide layers: yttrium iron garnets onto GaAs. *Appl. Phys. Lett.* **71**, 2617–2619 (1997).
183. Fichtner, S., Wolff, N., Lofink, F., Kienle, L. & Wagner, B. AlScN: a III-V semiconductor based ferroelectric. *J. Appl. Phys.* **125**, 114103 (2019).
184. Liang, X. et al. A review of thin-film magnetoelastic materials for magnetolectric applications. *Sensors* **20**, 1532 (2020).
185. Schoen, M. A. W. et al. Ultra-low magnetic damping of a metallic ferromagnet. *Nat. Phys.* **12**, 839–842 (2016).
186. Emori, S. et al. Coexistence of low damping and strong magnetoelastic coupling in epitaxial spinel ferrite thin films. *Adv. Mater.* **29**, 1701130 (2017).
187. Li, R. F. et al. Anisotropic magnon spin transport in ultrathin spinel ferrite thin films—evidence for anisotropy in exchange stiffness. *Nano Lett.* **22**, 1167–1173 (2022).
188. Childress, L. & Hanson, R. Diamond NV centers for quantum computing and quantum networks. *MRS Bull.* **38**, 134–138 (2013).
189. Taminiau, T., Cramer, J., van der Sar, T., Dobrovitski, V. & Hanson, R. Universal control and error correction in multi-qubit spin registers in diamond. *Nat. Nanotechnol.* **9**, 171–176 (2014).
190. Fuchs, G., Burkard, G., Klimov, P. & Awschalom, D. A quantum memory intrinsic to single nitrogen-vacancy centres in diamond. *Nat. Phys.* **7**, 789–793 (2011).
191. Taylor, J. et al. High-sensitivity diamond magnetometer with nanoscale resolution. *Nat. Phys.* **4**, 810–816 (2008).
192. de Lange, G., Riste, D., Dobrovitski, V. & Hanson, R. Single-spin magnetometry with multipulse sensing sequences. *Phys. Rev. Lett.* **106**, 080802 (2011).
193. Rondin, L. et al. Magnetometry with nitrogen-vacancy defects in diamond. *Rep. Prog. Phys.* **77**, 056503 (2014).
194. Du, C. et al. Control and local measurement of the spin chemical potential in a magnetic insulator. *Science* **357**, 195–198 (2017).
195. Hensen, B. et al. Loophole-free Bell inequality violation using electron spins separated by 1.3 kilometres. *Nature* **526**, 682–686 (2015).
196. Kikuchi, D. et al. Long-distance excitation of nitrogen-vacancy centers in diamond via surface spin waves. *Appl. Phys. Exp.* **10**, 103004 (2017).
197. Andrich, P. et al. Long-range spin wave mediated control of defect qubits in nanodiamonds. *Npj Quantum Inform.* <https://doi.org/10.1038/s41534-017-0029-z> (2017).
198. Stojanovic, M. Underwater acoustic communications. In *Proc. Electro/International 1995* 435–440 (IEEE, 1995).
199. Luo, H. et al. Recent progress of air/water cross-boundary communications for underwater sensor networks: a review. *IEEE Sens. J.* **22**, 8360–8382 (2022).
200. Yao, Z., Wang, Y., Keller, S. & Carman, G. Bulk acoustic wave-mediated multiferric antennas: architecture and performance bound. *IEEE Trans. Antennas Propag.* **63**, 3335–3344 (2015).

## Acknowledgements

The financial supports from the NSF TANMS ERC Award 1160504, NIH Award 1U1F1NS107694, W.M. Keck Foundation, US Army Combat Capabilities Development Command Aviation & Missile Center, and Winchester Technologies, LLC via SBIR/STTR Awards are gratefully acknowledged. A portion of this work used resources at Sandia National Laboratories. Sandia National Laboratories is a multimission laboratory managed and operated by National Technology & Engineering Solutions of Sandia, LLC, a wholly owned subsidiary of Honeywell International Inc., for the US Department of Energy's National Nuclear Security Administration under contract DE-NA0003525. This paper describes objective technical results and analysis. Any subjective views or opinions that might be expressed in the paper do not necessarily represent the views of the US Department of Energy or the US Government. The work at Rice is supported by the ARO-CHARM programme.

## Author contributions

B.L., A.R.W.-C., C.D., Y.H. and R.H. researched data for the article. B.L., A.R.W.-C., H.L., X.S., M.M., M.P., M.S. and N.X.S. contributed substantially to discussion of the content. B.L., A.R.W.-C., C.D., Y.H., X.L., R.R. and N.X.S. wrote the article. B.L., A.R.W.-C., R.R. and N.X.S. reviewed and/or edited the manuscript before submission.

## Competing interests

N.X.S. has a financial interest in Winchester Technologies LLC. The other authors declare no competing interests.

## Additional information

**Peer review information** *Nature Reviews Electrical Engineering* thanks Shad Roundy, Jungho Ryu and the other, anonymous reviewer(s) for their contribution to the peer review of this work.

**Publisher's note** Springer Nature remains neutral with regard to jurisdictional claims in published maps and institutional affiliations.

Springer Nature or its licensor (e.g. a society or other partner) holds exclusive rights to this article under a publishing agreement with the author(s) or other rightsholder(s); author self-archiving of the accepted manuscript version of this article is solely governed by the terms of such publishing agreement and applicable law.